Detection of Surface Submesoscale Fronts in the Atlantic Ocean

Qian Liu[123], Dante C. Napolitano[4], Jonathan Gula[4], Mengjiao Wang[123], Yingjie Liu[123], Le Gao[123], Xiaofeng Li[123]*

[1] Key Laboratory of Ocean Observation and Forecasting & Laboratory of Ocean Circulation and Waves, Institute of Oceanology, Chinese Academy of Sciences, Qingdao, 266400, China.

[2] Laboratory for Ocean Dynamics and Climate, Qingdao Marine Science and Technology Center.

[3] University of Chinese Academy of Sciences, Qingdao, 266400, China.

[4] Univ. Brest, CNRS, IRD, Ifremer, *Laboratoire d'Océanographie Physique et Spatiale* (LOPS), IUEM, 29280, Brest, France.

*Corresponding author: Xiaofeng Li (lixf@qdio.ac.cn)

Abstract

Submesoscale fronts are narrow zones of sharp tracer gradients. They play a significant role in upper-ocean dynamics, vertical exchanges, and biogeochemical processes. However, detecting submesoscale fronts across ocean basins is challenging due to observational limitations and the complexity of frontogenesis processes. This study examines tracer- and velocity-based diagnostics for detecting surface submesoscale fronts using a submesoscale-permitting Atlantic simulation. The Local Variability Index (LVI) identifies thermal, haline, and density fronts, and the Finite-Time Lyapunov Exponent (FTLE) identifies dynamical fronts. All types of fronts have stronger strain, vorticity, convergence, and frontogenesis than the background, with dynamical and density fronts showing the strongest signatures. Dynamical fronts are the most spatially widespread, whereas the distribution of density fronts reflects the combined influence of deformation-driven frontogenesis and thermohaline compensation or reinforcement. Density fronts often co-occur with dynamical and thermohaline fronts, consistent with deformation-driven frontogenesis. FTLE identifies density fronts more effectively than temperature-based LVI in salinity-dominated regions and more effectively than salinity-based LVI in temperature-dominated regions. However, FTLE may also capture elongated deformation features that are spatially offset from instantaneous density fronts, especially where compensation weakens buoyancy gradients. Combining FTLE and LVI enables a more comprehensive detection of density fronts across diverse dynamical regions. FTLE remains effective at mesoscale resolving resolution (~12.5 km) but decreases noticeably at altimetry-like effective resolution (~100 km). LVI requires high-resolution satellite-based data to capture submesoscale variability. This work provides new insights into spatial and seasonal variability of submesoscale fronts and benchmarks front-detection methods in high-resolution simulations and observations.

Keywords: Submesoscale, Front, Finite-time Lyapunov exponent, F1-score, Thermohaline compensation, Atlantic

1 Introduction

Submesoscale fronts are narrow zones marked by sharp horizontal gradients in temperature, salinity, density, or other tracers, and typically exhibit spatial scales of 1–10 km and a lifespan of 1–10 days (Lévy et al., 2023; McWilliams, 2016, 2019; Taylor & Thompson, 2023). They are characterized by $O(1)$ Rossby and Richardson numbers (Balwada et al., 2021; Barkan et al., 2019; Thomas et al., 2008). The departures from geostrophic balance allow strong vertical velocities to develop. By modulating vertical and lateral fluxes of momentum, heat, and tracers, submesoscale fronts play a central role in upper-ocean stratification, mixing, biological productivity, air-sea interactions, and the energy cascade from larger to smaller scales (Freilich et al., 2022; Lévy et al., 2018; Mahadevan, 2016; Strobach et al., 2022; Zhang et al., 2023). Their ubiquity and dynamical influence in the upper-ocean make them a key target for advancing ocean modeling and understanding fine-scale ocean processes.

The generation and evolution of submesoscale fronts involve a variety of processes, among which frontogenesis typically plays a leading role in sharpening and maintaining frontal structures. Frontogenesis disrupts the geostrophic balance at fronts, inducing an ageostrophic secondary circulation (Mahadevan et al., 2020; McWilliams, 2021; Taylor & Thompson, 2023). This generates vertical velocities that are an order of magnitude larger than those driven by mesoscale eddies, reaching up to 10–100 m day^{-1} (Gula et al., 2022; Klein & Lapeyre, 2009). In addition to frontogenesis, submesoscale fronts are influenced by various other mechanisms, such as mixed-layer baroclinic instability, symmetric instability, ageostrophic anticyclonic instability, and horizontal shear instability (Boccaletti et al., 2007; D'Asaro et al., 2011; Gula et al., 2022; McWilliams et al., 2004; Munk et al., 2000; Thomas & Taylor, 2010). Commonly, these processes occur simultaneously and their relative contributions to frontal evolution vary geographically and seasonally (Callies et al., 2015; Rocha et al., 2016; Sasaki et al., 2014). Submesoscale fronts are challenging to investigate theoretically, observationally, and numerically, owing to the interactions among multiple dynamical processes and the short spatiotemporal scales of submesoscale fronts (Barkan et al., 2019). This motivates sustained efforts to identify them robustly using *in situ* observations, satellite remote sensing, and numerical models.

Difficulties in measuring intermittent submesoscale dynamics restrict *in situ* observational studies to a few well-sampled regions via ship-based measurements (Adams et al., 2017; Poje et al., 2014; Thompson et al., 2016; Yu et al., 2024) and high-frequency (HF) radar observations (Archer et al., 2015; Yoo et al., 2018). Recently, Whalen and Drushka (2025) used global ship-based thermosalinograph measurements to detect submesoscale density fronts, defined as sequences of at least 4 consecutive points with consistent density gradients exceeding 10^{-5} kg m^{-4}. They provide global perspective on the variability and dynamics of submesoscale fronts. However, the spatiotemporal coverage is limited, with observations predominantly confined to the Northern Hemisphere and austral summer. They also recognized that some conclusions are not statistically significant in the Southern Hemisphere. Furthermore, the dataset only provides frontal width and strength, while lacking information on the frontal area.

With the improvement of spatiotemporal coverage and resolution, satellite remote sensing has been widely used to identify submesoscale fronts. Various diagnostics have been developed to identify submesoscale fronts, including imagery-based indices, dynamical criteria, and Lagrangian methods, each emphasizing a different aspect of frontal dynamics. For example, Liu and Levine (2016) proposed the Heterogeneity Index (HI) to identify surface submesoscale fronts using daily sea surface temperature (SST) data at 1 km resolution in the North Pacific Subtropical Gyre. HI

combines the variance, skewness, and bimodality of SST distributions computed within a 10 × 10 pixel sliding window. Compared to traditional gradient-based methods, HI captures submesoscale signals while remaining less sensitive to noise. At the same time, an inherent limitation of SST-based detection is that it may miss fronts with weak thermal contrasts (e.g., salinity-compensated density fronts). Zhang et al. (2019) defined fronts as locations where the local strain rate is maximum, with the geostrophic strain rate surpassing 1.0×10^{-5} s^{-1} in the direction of the geostrophic current. Using the dynamical criteria, they directly combined frontal kinematics with drifter-based chlorophyll tendencies and revealed that ageostrophic secondary circulation induces upwelling on the light side of fronts, promoting surface chlorophyll growth. Nevertheless, this approach is constrained by the effective resolution of altimetry-derived geostrophic fields.

Lagrangian diagnostics, especially the Finite-Time Lyapunov Exponent (FTLE) and Finite-Size Lyapunov Exponent (FSLE), have emerged as powerful tools for detecting submesoscale fronts (Fahlbusch et al., 2024; Guo et al., 2019). Both diagnostics quantify particle separation in a flow field, but differ in formulation: FTLE quantifies the rate at which initially neighboring particles separate over a fixed time interval, whereas FSLE is inversely proportional to the time required for two initially close particles to separate to a prescribed distance (Allshouse & Peacock, 2015a; d'Ovidio et al., 2004; Hadjighasem et al., 2017; Lapeyre, 2002; Ott, 2002; Ottino, 1989). Maxima in backward-time FTLE and FSLE (called ridges) correspond to attracting Lagrangian Coherent Structures (LCSs), which act as transport barriers and often coincide with surface convergence zones and submesoscale filaments (Gough et al., 2016; Huntley et al., 2011; Lehahn et al., 2007). These structures delineate frontal boundaries and strongly influence tracer distribution. Compared to traditional Eulerian diagnostics, Lagrangian methods can uncover hidden transport structures and fine-scale patterns shaped by chaotic advection, making them invaluable for studying the complex and transient nature of submesoscale dynamics (Aravind et al., 2023; Calil & Richards, 2010; Cotté et al., 2015; d'Ovidio et al., 2009; Hernández-Carrasco et al., 2011). For instance, Guo et al. (2019) used FSLE derived from altimetric velocities to diagnose submesoscale filaments associated with mesoscale horizontal shear and strain deformation. However, the ability of FSLE and FTLE to reveal submesoscale transport structures depends on the accuracy and spatial resolution of the underlying velocity field. Present altimetry or reanalysis products typically do not fully resolve 1–10 km submesoscale features.

Although high-resolution satellite SST and ocean color products can been used to detect frontal structures, they provide only partial information on frontal dynamics, since temperature signals may be salinity-compensated (Spiro Jaeger & Mahadevan, 2018), and ocean color is a nonconservative tracer (Zhang et al., 2019). In contrast, density fronts provide a more reliable measure of frontal dynamics, directly reflecting water mass boundaries and movement. Density variations control stratification intensity and determine whether the local water column is susceptible to vertical perturbations and mixing (Dave & Lozier, 2010). Density fronts are often associated with frontogenesis, leading to upwelling on the light side and downwelling on the dense side of the front (McWilliams, 2021). These circulations modify the density profile, regulate the stratification structure and local stability, and thereby influence the exchange of energy, matter, and momentum between the surface and subsurface layers (Liu et al., 2025). At present, the limited availability and coarse resolution of salinity observations hinder direct observation of submesoscale density structures, motivating the use of high-resolution numerical simulations to investigate their dynamics and impacts. In such simulations, frontal detection is commonly achieved by computing horizontal gradients of temperature, salinity, or density and applying fixed

thresholds such as the 90th or 95th percentile (e.g., Duan et al., 2024; Spiro Jaeger & Mahadevan, 2018).

In this study, we use a realistic, submesoscale-permitting Atlantic Ocean numerical simulation with kilometer-scale resolution to systematically evaluate and compare commonly applied diagnostics for identifying submesoscale fronts from observations, including FTLE and Local Variability Index (LVI, a method based on HI). Specifically, thermal, haline, and density fronts are identified using LVI computed from surface temperature, salinity, and density fields, respectively, whereas dynamical fronts are diagnosed using FTLE derived from the surface velocity field. Previous work has shown that FTLE and FSLE can yield comparable results in numerical flow visualization when appropriately parameterized (Haller, 2015; Karrasch & Haller, 2013; Peikert et al., 2014). However, FSLE can exhibit jump discontinuities, making it sensitive and less robust in nonlinear flows and potentially degrading the accuracy of FSLE statistics (Haller, 2023, Section 5.2.8). It can also be ill-posed for certain separation ratios and becomes insensitive to further flow evolution once the separation time is reached (Karrasch & Haller, 2013). From a multiscale perspective, FSLE better characterizes large-scale transport structures, whereas FTLE is more sensitive to finer-scale features of particle dispersion (Boffetta et al., 2001). Moreover, FTLE is more computationally efficient, as it requires only a single precomputed flow map. Therefore, we choose FTLE for the subsequent analysis. In addition, we investigate the relationship between thermal, haline, and dynamical fronts relative to density fronts, to assess the potential limitations and uncertainties when using satellite SST and velocity fields to identify fronts.

This study provides a comprehensive benchmark for surface submesoscale front detection and reveals regional and seasonal contrasts in frontal occurrence, intensity, and dominant type. The paper is structured as follows: Section 2 describes the data and methodology; Section 3 presents the characteristics of submesoscale fronts; Section 4 explores the relationship between dynamical, thermal, and haline fronts relative to density fronts; Section 5 evaluates the performance of FTLE derived from the coarse velocity; and Section 6 concludes the study.

2 Data and methods

2.1 Numerical simulation

This study utilizes the temperature, salinity, and velocity fields of the GIGATL1 simulation (Gula et al., 2021), a submesoscale-permitting Atlantic-wide (107°W–31°E, 56°S–74°N, Figure 1) simulation performed with the Coastal and Regional Ocean COmmunity model (CROCO), developed from the Regional Ocean Modeling System (ROMS; Shchepetkin & McWilliams, 2005). The GIGATL1 grid is orthogonally constructed on an oblique Mercator projection to ensure near-uniform horizontal spacing. The grid resolution varies from 1 km near the central longitude to 735 m near the western and eastern edges. The model grid consists of 10,500 points in the zonal direction and 14,000 points in the meridional direction. It solves the hydrostatic primitive equations with a free surface, using a terrain-following vertical coordinate system with 100 sigma levels. The bathymetry is taken from the SRTM30plus dataset (Becker et al., 2009). Vertical mixing is parameterized using the k-ε turbulence closure scheme with the Canuto A stability function (Canuto et al., 2001; Umlauf & Burchard, 2003). No explicit lateral diffusion or viscosity is used. The effect of bottom friction is parameterized with a logarithmic law of the wall with a roughness length of 0.01 m.

The simulation is run from 02 July 2007 to 05 September 2009. It is initialized using fields from a coarser 3 km-resolution simulation (GIGATL3), with an identical setup (e.g., Ruan et al., 2021; Schubert et al., 2025; Vic et al., 2022). Boundary conditions are from Simple Ocean Data Assimilation (SODA; Carton & Giese, 2008). Atmospheric forcing is provided by hourly fields from the Climate Forecast System Reanalysis (CFSR), which employ a bulk formulation and a stress-correction approach to parameterize the feedback of surface ocean currents on the atmosphere (Renault et al., 2020). Simulations include barotropic tidal forcing at the boundaries, as well as tidal potential and self-attraction, which are derived from TPXO7.2 and GOT99.2b, respectively. The GIGATL1 simulation is included in the intercomparison of submesoscale-permitting realistic ocean models presented in Uchida et al (2022). It has recently been used in studies investigating mesoscale and submesoscale dynamics, including the ocean kinetic energy cascade (Schubert et al., 2023), vertical eddy fluxes (de Marez et al., 2025), and the near-inertial wave dynamics (Qu et al., 2021). For this study, we specifically analyze the daily-averaged temperature, salinity, and buoyancy of the GIGATL1 simulation for two representative months: June and December 2008, to examine potential seasonal contrasts in frontal activity. This choice is justified because a comparison between daily and hourly buoyancy gradients shows only a minor reduction in intensity, indicating that daily averages still capture the essential frontal signal (Figure S1). For FTLE discussed in Sections 3, 4, and 5, we used the hourly velocity fields.

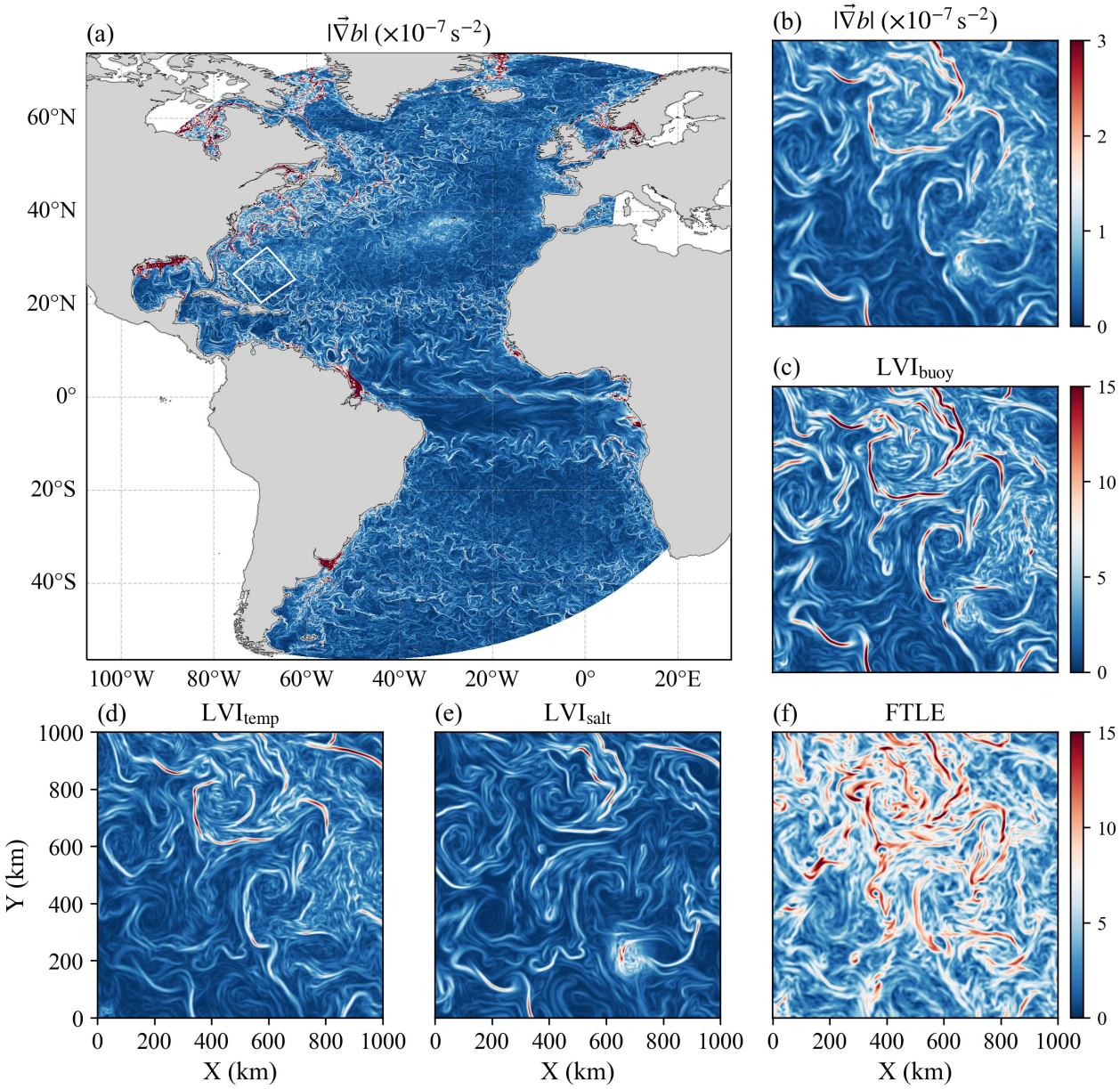

Figure 1. Horizontal buoyancy gradient and frontal diagnostics on 2 June 2008. (a) Horizontal buoyancy gradient in the Atlantic Ocean. The buoyancy gradient is defined as $\left|\vec{\nabla}b\right| = g\left|\vec{\nabla}\rho\right|/\rho_0$, where b is the buoyancy, g is gravity, ρ is surface density, and ρ_0 is the reference density of 1027 kg m^{-3}. The buoyancy gradient is smoothed using a uniform 11 × 11 km filter for comparison with the frontal diagnostics. Snapshots in the zoomed-in region of (b) $\left|\vec{\nabla}b\right|$, (c) LVI$_{buoy}$, (d) LVI$_{temp}$, (e) LVI$_{salt}$, and (f) FTLE.

2.2 From Heterogeneity Index to Local Variability Index

We apply the HI method proposed by Haëck et al. (2023) to detect surface submesoscale fronts. HI is defined as a weighted sum of skewness γ, standard deviation σ, and bimodality B to quantify the heterogeneity of sea surface properties. It is computed at each grid point within an 11 × 11-pixel square window, corresponding to a spatial scale of approximately 10 km in the

GIGATL1 configuration. This scale is chosen to isolate submesoscale features while avoiding observational noise.

Although HI has been applied to satellite SST data to identify thermal fronts, our analysis reveals two limitations when applied to high-resolution simulations. First, the bimodality component strongly depends on the choice of histogram bin width. Sensitivity analyses show that different bin widths yield substantial variations in the number, intensity, and continuity of detected fronts, rendering the bimodality component unreliable for quantitative front identification (see Text S1). Second, skewness tends to highlight isolated anomalies and small-scale noise, producing patchy or duplicated structures rather than coherent fronts (Text S2).

To avoid these issues, we apply a simplified and more robust metric, the Local Variability Index

$$\mathrm{LVI}_{\phi} = a \times (b\sigma_{\phi}), \text{ with } a = \frac{9.5}{P_{95}(b\sigma_{\phi})}. \quad (1)$$

σ_{ϕ} denotes the standard deviation of tracer ϕ within a sliding window centered at each pixel. b is the inverse of the standard deviation of σ_{ϕ} over the entire domain and full time series. P_{95} is the 95th percentile. a is a normalization coefficient to ensure that 95% of LVI_{ϕ} values are less than 9.5. LVI retains only the standard deviation component, which reliably captures coherent frontal structures across all tracers and is less affected by binning artifacts or outliers (Figure S5). Additionally, it reflects the magnitude of local variability, which is closely related to submesoscale gradients. Figure S7 compares LVI of buoyancy ($\mathrm{LVI}_{\mathrm{buoy}}$) with the buoyancy gradient. After smoothing the gradient at the same 10-km scale, the two fields exhibit nearly identical spatial patterns, with a Pearson correlation coefficient r = 0.97 computed over all data points.

Although LVI shows high spatial correspondence with smoothed gradients, it is adopted in this study because it directly targets variability at a prescribed spatial scale (~10 km), is more robust to observational noise, and provides a normalized framework for consistent comparison across different tracers. To further examine the performance of LVI and gradient-based methods to noise, we add Gaussian noise to the buoyancy field (Figure S8a). $|\vec{\nabla}b|$ becomes strongly contaminated by noise, as finite-difference gradients amplify the grid-scale variability (Figure S8c). Even after spatial filtering is applied to $|\vec{\nabla}b|$, residual small-scale artifacts remain, and the fronts detected from the filtered noisy $|\vec{\nabla}b|$ are more fragmented and show noisier edges than those obtained from the original field (Figure S9a). However, $\mathrm{LVI}_{\mathrm{buoy}}$ is less sensitive to noise and better preserves coherent frontal patterns (Figure S9b). When the diagnostics are computed from the filtered buoyancy field, the spatial correspondence between the gradient-based and LVI-based diagnostics becomes much closer (Figures S9c and S9d). However, $|\vec{\nabla}b|$ computed from the filtered noisy buoyancy field still retains residual small-scale variability, and the detected frontal boundaries are less smooth and less continuous than those obtained from LVI. This comparison further supports the use of LVI as a scale-aware diagnostic that better preserves coherent frontal structures in noisy buoyancy fields.

As a scale-dependent metric, LVI may weaken filament signatures that are much sharper than the chosen window. Accordingly, the window size should be adjusted to the target scale. In this study, submesoscale fronts are identified at a spatial scale of ~10 km scale, representative of

typical satellite resolution. Thus, the applicability of LVI depends on high-resolution data that resolve submesoscale variability. The LVI method is applied to sea surface temperature, salinity, and density fields to detect thermal, haline, and density fronts, respectively (Figures 1c–1e and S10). This consistent framework enables comparative analyses of frontal structures across multiple tracers at submesoscale resolution.

2.3 Finite-Time Lyapunov Exponent

Backward-time and forward-time FTLE ridges indicate the directions of horizontal stretching and compressing, respectively (Figure S11). The backward-time FTLE often delineates attracting LCSs, which are associated with surface frontal zones characterized by convergent flows and tracer sharpening. Therefore, in this study, the term "FTLE" will correspond to backward-time FTLE, unless specified otherwise.

At each initial position $\mathbf{x}_0$ and time t_0, the FTLE over an integration time T is defined as

$$\mathrm{FTLE}_{t_0}^{t_0-T}(\mathbf{x}_0) = \frac{1}{|T|} \ln\left(\sqrt{\lambda_{\max}(\mathbf{C}(\mathbf{x}_0, t_0)}\right), \tag{2}$$

where $\lambda_{\max}$ is the maximum eigenvalue of the right Cauchy–Green deformation tensor,

$$\mathbf{C}(\mathbf{x}_0, t_0) = \left(\nabla\Phi_{t_0}^{t_0-T}(\mathbf{x}_0)\right)' \nabla\Phi_{t_0}^{t_0-T}(\mathbf{x}_0). \tag{3}$$

$\Phi_{t_0}^{t_0-T}$ is the flow map which gives the final position of a fluid parcel initially at $\mathbf{x}_0$, after advection over the time interval T. The flow map depicts the flow directions and particle movements.

To construct the flow map $\Phi_{t_0}^{t_0-T}$, we use a standard fourth-order Runge–Kutta method with an integration time step dt = 2 h. We obtained the trajectory $\mathbf{x}$ ($t_0 - T$) by numerically integrating the velocity field over a finite time interval T = 24 h. We interpolate the velocity data using a bilinear interpolation scheme. The interpolation procedure for the non-uniform grid is described in Text S3.

To compute the gradient of the flow map $\nabla\Phi$, four auxiliary particles are initialized at an initial separation δ_0 = 1 km in the x and y directions around each particle, which is located at $\mathbf{x}_0$ at time t_0. Their final positions after advection are used to compute the components of the Jacobian matrix via centered finite differences,

$$\nabla\Phi = \begin{bmatrix} \dfrac{x^{(+\delta_x)} - x^{(-\delta_x)}}{2\delta_x} & \dfrac{x^{(+\delta_y)} - x^{(-\delta_y)}}{2\delta_y} \\ \dfrac{y^{(+\delta_x)} - y^{(-\delta_x)}}{2\delta_x} & \dfrac{y^{(+\delta_y)} - y^{(-\delta_y)}}{2\delta_y} \end{bmatrix}, \tag{4}$$

where superscripts indicate perturbations in the X and Y directions, respectively. Instead of using the four nearest neighbors on the computational grid, this setup ensures accurate estimation of the local deformation gradient, especially under non-uniform grid configurations. For example, as shown in Figure S12, computing $\nabla\Phi$ using auxiliary particles with fixed spacing yields clearer filamentary and vortical structures. The boundaries of submesoscale features appear sharper and fine structural details are more evident. However, using the nearest grid-based neighbors produces more blurred structural boundaries, with many small-scale eddies and fronts being smoothed out and less discernible.

FTLE is sensitive to the initial separation distance δ_0. In theory, FTLE describes the separation of infinitesimally close particles over a finite time. In practice, however, δ_0 cannot be chosen arbitrarily small in discrete velocity fields (Günther et al., 2016). Numerical errors are observed when the auxiliary grid points used for the finite-difference approximation become indistinguishable from each other (Allshouse & Peacock, 2015b). The effects of numerical errors and velocity noise on FTLE fields become more pronounced at smaller grid spacing (Fang et al., 2020). Such effects are also observed in this study. For example, when δ_0 = 0.0001 km, the resulting FTLE fields exhibit typical "salt-and-pepper" noise (Rafiee & Farhang, 2023), characterized by isolated pixel-scale dots superimposed on the FTLE field (Figure S13a). Conversely, choosing a too large δ_0 smears FTLE ridges and reduces spatial resolution (Figure S13c). Balancing these considerations, we set δ_0 = 1 km for the FTLE calculations, which is consistent with the approximate spatial resolution of the velocity field. This choice suppresses numerical errors while preserving the main LCSs, yielding results comparable to those obtained using δ_0 = 0.0001 km when the salt-and-pepper noise is ignored.

Another key scale factor affecting the FTLE is the integration time T, because FTLE quantifies the particle separation rate over a finite time interval. When T is short, the FTLE captures local, short-term stretching, making it sensitive to small-scale, transient flow features. As T increases, fine-scale structures become weaker and less distinct. For example, at T = 120 h, only strong, persistent structures remain, while finer details are smoothed out (Figure S13f). Therefore, we choose an intermediate value, T = 24 h, to retain submesoscale filaments while suppressing short-lived noise.

Apart from the integration duration, the integration time step dt used during trajectory computation also affects the FTLE results. A large dt (e.g., 10h) may introduce integration errors, leading to spatial distortions, as shown in Figure S13i. Even though the velocity field is available at 1 h intervals, we choose an integration time step dt = 2 h to reduce computation time while achieving accurate resolution of submesoscale structures (Figure S13h). Additionally, the mean difference in final positions between dt = 2 h and dt = 1 h is 0.94 km. When normalized by the trajectory length, the mean trajectory error is 0.045. These errors are small relative to the grid spacing (1 km) and the target submesoscale scale (~10 km), indicating that dt = 2 h provides sufficient numerical accuracy. Details of this assessment are described in Text S4.

To extract frontal structures at 10-km scales, we first smooth the FTLE fields using an 11 × 11 mean filter, consistent with the LVI computation. Then we normalize the FTLE values following the same procedure (used for LVI),

$$\mathrm{FTLE}_{norm} = a \times (b \times \mu_{\mathrm{FTLE}}),\ b = \frac{1}{\mathrm{std}(\mu_{\mathrm{FTLE}})_{\mathrm{total}}},\ a = \frac{9.5}{P_{95}(b \times \mu_{\mathrm{FTLE}})}, \tag{5}$$

where μ_{FTLE} denotes the mean FTLE value within an 11 × 11 window. $(\mu_{\mathrm{FTLE}})_{\mathrm{total}}$ includes all FTLE data across the study period, and P_{95} is the 95th percentile of $b \times (\mu_{\mathrm{FTLE}})_{\mathrm{total}}$, indicating that 95% of FTLE values fall below 9.5. FTLE discussed in Sections 3, 4, and 5 is the normalized FTLE. A zoomed snapshot of the FTLE field is shown in Figure 1f.

2.4 Submesoscale front extraction using filters and thresholds

Previous studies often relied on fixed thresholds to delineate frontal regions (Barceló-Llull et al., 2021; Duan et al., 2024). However, when applied over basin scales, such thresholds may fail

in areas where tracer gradients are particularly strong. To resolve this issue, we progressively apply temporal and spatial filters to isolate submesoscale signals. Figure S15 compares the effects of thresholding, temporal filtering, spatial filtering, and their combination on frontal extraction.

Using the Mississippi Plume as an example, applying the 90th-percentile LVI_{buoy} threshold derived from the whole Atlantic produces unrealistically broad frontal zones that obscure the narrow, filamentary morphology characteristic of submesoscale fronts (Figure S15a). We perform a temporal filtering on LVI_{buoy} by removing a 10-day moving average (Wang et al., 2025). Positive anomalies from the temporally filtered field are used as a mask for the original LVI_{buoy}, suppressing weak signals and improving frontal-zone localization (Figure S15b). However, the boundaries between adjacent fronts remain indistinct. A high-pass Gaussian spatial filter (cutoff = 30 km) improves this separation by removing mesoscale contributions (Figure S15c). Previous studies commonly apply spatial filtering after temporal filtering (Gaube et al., 2015; Liu et al., 2023). One can see that the result of this combined filtering is similar to spatial filtering but retains more residual weak signals (Figure S15d).

Temporal and spatial filtering act to extract signals at specific scales in their respective dimensions. To ensure consistency with submesoscale temporal and spatial scales, we construct two masks from the time- and space-filtered fields (>0). In addition, we introduce a third mask based on the 90th-percentile threshold to identify regions of strong tracer gradients (Figure S15f). We also apply the same masking strategy to LVI of temperature (LVI_{temp}), LVI of salinity (LVI_{salt}), and FTLE (Figure S16).

3 Characteristics of submesoscale fronts in the Atlantic Ocean

3.1 Submesoscale diagnostics and frontogenesis

To investigate how dynamical processes deform the flow and generate fronts, we analyze key kinematic quantities derived from the velocity gradient tensor, including the strain magnitude (σ), vertical vorticity (ζ), and horizontal divergence (δ), defined as:

$$\sigma = \sqrt{(u_x - v_y)^2 + (v_x + u_y)^2},\ \zeta = v_x - u_y,\ \delta = u_x + v_y. \tag{6}$$

In this study, σ and δ are normalized by the absolute value of Coriolis frequency $|f|$, and ζ is normalized by f. Normalization provides dimensionless measures relative to planetary rotation, highlighting the role of ageostrophic motions in governing frontal evolution (Capet et al., 2008; Luko et al., 2023; Napolitano et al., 2021; Shcherbina et al., 2013; Thomas et al., 2008).

Frontogenesis describes the intensification of horizontal density gradients, which can be driven by mesoscale straining, the nonlinear evolution of baroclinic instability, and interactions between fronts and small-scale turbulence within the turbulent thermal wind (TTW) framework (Gula et al., 2014; McWilliams et al., 2015; Sullivan & McWilliams, 2018; Verma et al., 2019). The frontogenesis function quantifies this process by isolating the advective contribution to the evolution of the horizontal buoyancy gradient (Hoskins, 1982),

$$F = \frac{D|\nabla_h \rho|^2}{Dt}, \tag{7}$$

which can be separated into several components. In this study, we neglect the vertical advection and diabatic terms, focusing on the horizontal advective contribution.

$$F_h = \mathbf{Q}_h \cdot \nabla_h \rho, \text{ with}$$
$$\mathbf{Q}_h = -\left(u_x \rho_x + v_x \rho_y\right)\mathbf{i} - \left(u_y \rho_x + v_y \rho_y\right)\mathbf{j}. \quad (8)$$

In (8), F_h quantifies the growth rate of the horizontal density gradient driven by horizontal straining. To better compare frontogenesis efficiency across different regions and tracers, we define a nondimensional measure following Barkan et al. (2019),

$$F_s = \frac{F_h}{f\,|\nabla_h \rho|^2}. \quad (9)$$

Positive F_s correspond to frontogenesis, while negative values correspond to frontolysis. To avoid the singularity as the Coriolis parameter approaches zero, regions within ±5° latitude are excluded from the analysis.

We calculate the probability density functions (pdfs) of $\sigma/|f|$, ζ/f, $\delta/|f|$, and F_s over different frontal zones, including dynamical (FTLE), density (LVI_{buoy}), thermal (LVI_{temp}), and haline (LVI_{salt}) fronts. Compared to the background, all front types have stronger dynamical activity, including deformation, rotation, convergence/divergence, and frontogenesis/frontolysis (Figure 2). Moreover, there is a distinct asymmetry skewed toward cyclonic vorticity, convergence, and frontogenesis, which is a typical feature of submesoscale fronts (Balwada et al., 2021; Barkan et al., 2019; Hetland et al., 2025; Shcherbina et al., 2013). The cyclonic skewness of the vorticity field arises from the asymmetric response of vorticity tendency to vortex stretching (McWilliams, 2016). These results are consistent with previous studies, suggesting that FTLE and LVI are capable of capturing key dynamical features of submesoscale fronts.

Compared to thermal and haline fronts, dynamical and density fronts occur more frequently at larger strain, vorticity, convergence, and frontogenesis (σ, ζ, $-\delta$, and $F_s \geq f$; Figure 2). This reflects their closer link to deformation-driven frontogenesis. In strain-dominated and confluent regions, cross-front compression and along-front stretching sharpen lateral buoyancy gradients, promoting the formation of density fronts (Hoskins, 1982). Additionally, convergence in such regions facilitates the aggregation of tracer gradients and enhances the vertical tilt of isopycnals, both of which contribute to frontogenesis. The cross-front compression, convergence, and horizontal shear can enhance vertical relative vorticity (Figure 2f). With FTLE consistently capturing these features as attracting LCSs, the pdfs of density and dynamical fronts show a nearly identical distribution when $\sigma/|f| > 0.5$ and $\zeta/f > 0.2$. By contrast, thermal and haline fronts are more directly influenced by surface forcing processes such as heating, evaporation, precipitation, and vertical mixing. Moreover, frontal dynamics are primarily governed by density, whereas the dynamical relevance of thermal and haline fronts depends on their contributions to density variations. When density compensation in opposing temperature and salinity gradients reduces the net buoyancy gradients (Rudnick & Ferrari, 1999), frontogenesis and the associated dynamical response are weakened.

Interestingly, the probability density distribution of dynamical fronts is more similar to haline fronts than density fronts in terms of $\delta/|f|$ (Figure 2g). This similarity may reflect the fact that haline fronts are typically more surface-intensified, primarily influenced by evaporation–precipitation, river discharge, or sea ice melting and freezing, and are often associated with shallow mixed layers where salinity dominates density (Spiro Jaeger & Mahadevan, 2018; Wilson & Riser,

2016). These fronts tend to produce strong and persistent surface convergence, which may be well captured by the time-integrated nature of FTLE.

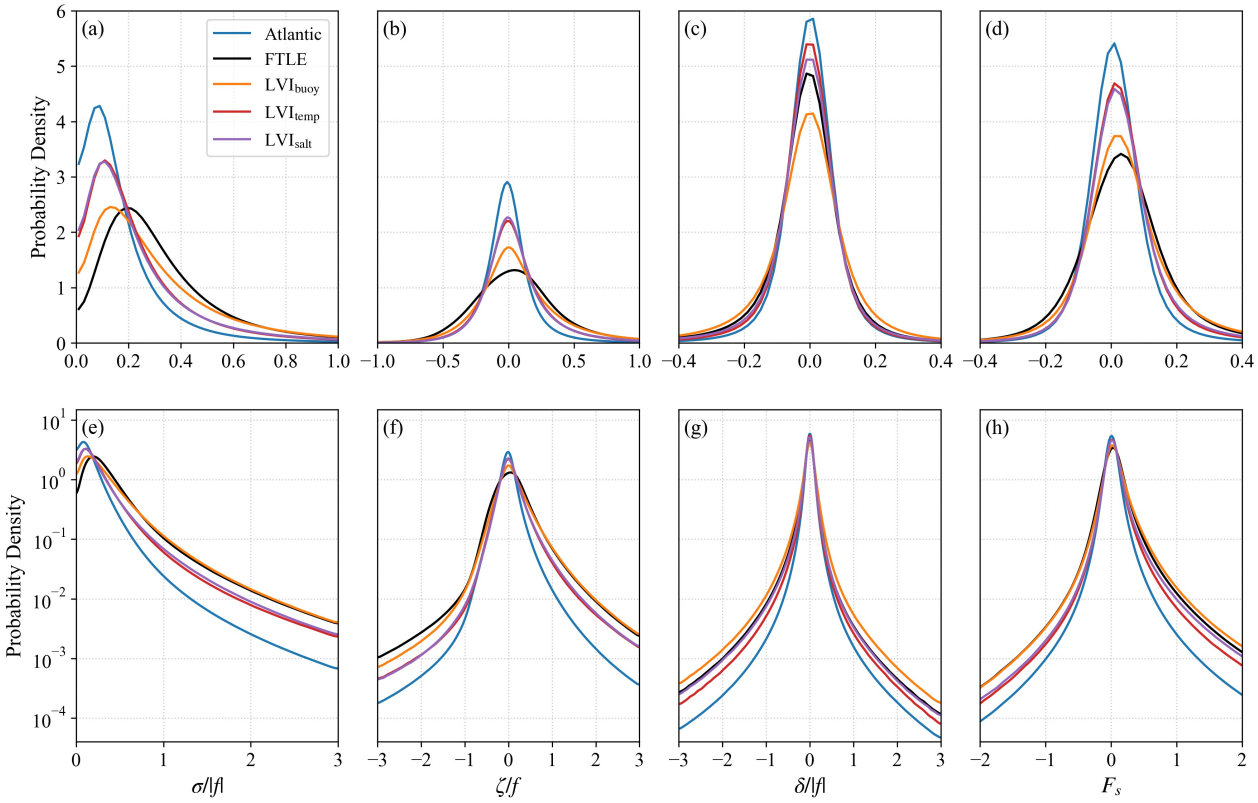

Figure 2. Probability density functions of normalized dynamical variables for the Atlantic background (blue) and submesoscale fronts identified by FTLE (black), LVI_{buoy} (orange), LVI_{temp} (red), and LVI_{salt} (purple). (a–d) use a linear y-axis, and (e–h) use a logarithmic y-axis. Variables: (a, e) $\sigma/|f|$, (b, f) ζ/f, (c, g) $\delta/|f|$, (d, h) F_s.

3.2 Spatial and seasonal patterns of submesoscale fronts in the Atlantic Ocean

We distinguish four complementary diagnostics that represent different aspects of submesoscale frontogenesis. Density fronts (LVI_{buoy}) provide the most direct measure of submesoscale frontal dynamics. Thermal and haline fronts (LVI_{temp}, LVI_{salt}) identify regions where buoyancy gradients are primarily dominated by temperature or salinity. Dynamical fronts diagnosed by backward-time FTLE correspond to Lagrangian stretching and convergence structures that can sharpen existing thermohaline gradients. Thermohaline compensation, together with the potential spatial offset between FTLE structures and buoyancy-gradient sharpening, can result in substantial differences in the spatial coverage and seasonal variability among different front types. As a baseline for the subsequent co-occurrence and performance analyses, we quantify the frequency and strength of each front type across the Atlantic. Seasonal means are computed with summer defined as June in the Northern Hemisphere and December in the Southern Hemisphere, and vice-versa for winter. Here, frequency is defined as the fraction of days with detected fronts relative to the total number of days in a given month. The strength of fronts represents the monthly mean of the magnitude of LVI_{ϕ} and FTLE, normalized beforehand and therefore a dimensionless quantity.

Regions where all front types co-occur with both high frequency and intensity are primarily observed in western boundary currents and extensions, such as the Gulf Stream (GS) and the Brazil–Malvinas Confluence (BMC), as well as in the subtropical–subpolar transition zones (Figures 3). These regions coincide with stronger tracer gradients, velocity speed, strain, and relative vorticity (absolute value) than the tropical Atlantic interior (about 10°–20°N/S) and subtropical gyre interiors (20°–40°N/S; Figures S18 and S19; Table S1). In the latter regions, fronts of all types are sparse.

Dynamical fronts are widespread across the basin, with high frequencies not only in regions where all front types co-occur but also in the Benguela Current, Canary Current, the equatorial currents, and the subtropical gyre (Figures 3a and 3b). Compared to thermal and haline fronts, dynamical fronts show broader spatial coverage and more uniform intensity patterns (Figures S17a and S17e). This is because FTLE identifies attracting transport structures associated with flow deformation and particle convergence. Such deformation can be generated by mesoscale currents and eddies, while their convergent branches promote tracer accumulation and frontal sharpening at smaller scales (Chelton et al., 2011; McWilliams, 2016). Consequently, dynamical fronts are less constrained by local temperature and salinity contrasts than thermal and haline fronts.

Density fronts are also concentrated near coastal regions and river-influenced zones (e.g., the Amazon-Orinoco, Congo, and Niger plumes), where buoyancy gradients driven by freshwater input dominate (Figures 3c and 3d). Their intensities are strongest in the Labrador Sea, the North Atlantic subpolar gyre, and along western boundary current extensions (Figures S17b and S17f). In the Labrador Sea and subpolar gyre, strong density fronts are supported by large-scale thermohaline structure associated with deep convection and water-mass transformation. Along western boundary current extensions, enhanced frontal intensity is more directly linked to mesoscale strain and frontogenesis driven by eddy–jet interactions.

The most distinctive feature of thermal fronts is their sparse distribution between 20°S and 20°N, which is consistent with the observational thermal fronts (Figure 4c in Xing et al., 2025). In the equatorial zone, uniform heating from intense solar shortwave radiation homogenizes the surface temperature field (Xing et al., 2023). Strong stratification and weak mesoscale dynamics suppress the development of thermal fronts (Liu et al., 2021). In contrast, strong thermal fronts are observed in the North Atlantic Subpolar Front Zone (45°–60°N), the South Atlantic westerly wind belt (40°–55°S), and along the eastern boundary upwelling regions such as the southwestern African coast and the Canary Current. These pronounced fronts result from sharp thermal contrasts between distinct water masses, which arise from different physical processes across regions. In subpolar regions, strong horizontal temperature gradients are maintained by large-scale circulation and intense air–sea heat fluxes (Large & Yeager, 2009; Marshall & Schott, 1999). In the Southern Ocean, sharp thermal gradients are shaped by strong wind forcing and further intensified by strain associated with energetic mesoscale eddy activity (Liu et al., 2021; Thomas et al., 2008). Along eastern boundary systems, coastal upwelling brings cold subsurface waters to the surface, generating strong cross-shore temperature contrasts (Bakun, 1990; Chavez & Messié, 2009).

Unsurprisingly, haline fronts show strong spatial correspondence with major river outflows and regions of evaporative concentration (Figures 3g and 3h). A prime example is the Amazon-Orinoco River plume, where a pronounced haline front forms at the river–ocean interface (Coadou-Chaventon et al., 2024). Here, the front is particularly strong and frequent during the boreal summer (June), reflecting the seasonal peak in river discharge. The freshwater is advected northwestward along the Brazilian Shelf by the North Brazilian Current and spread outward into

the western equatorial Atlantic Ocean. In December, the Amazon plume weakens, and haline fronts become more dominant in subtropical gyres where evaporation drives salinity gradients.

Seasonal variability of frontal frequency and strength further reflects how different frontal diagnostics respond to seasonal forcing (Figures 3i and 3j). Dynamical fronts exhibit a pronounced seasonal cycle in frequency, with substantially higher occurrence during winter than summer, reflecting the enhancement of mesoscale and submesoscale stirring due in part to the presence of mixed-layer instabilities under stronger wintertime forcing (Callies et al., 2015). Their intensity, however, remains relatively stable across seasons. For thermal fronts, the frequency increases significantly during winter, due to intensified surface cooling that enhances near-surface temperature gradients. Regions with shallower mixed layers cool more efficiently than deeper-mixed-layer regions, increasing the cross-front temperature contrast (Spiro Jaeger & Mahadevan, 2018; Tozuka & Cronin, 2014). Haline fronts show higher frequency and strength during summer near riverine sources but become more widespread during winter in subtropical regions as evaporation strengthens. Density fronts are slightly more active and stronger in summer, but mostly in coastal regions due to the seasonal cycle of freshwater input.

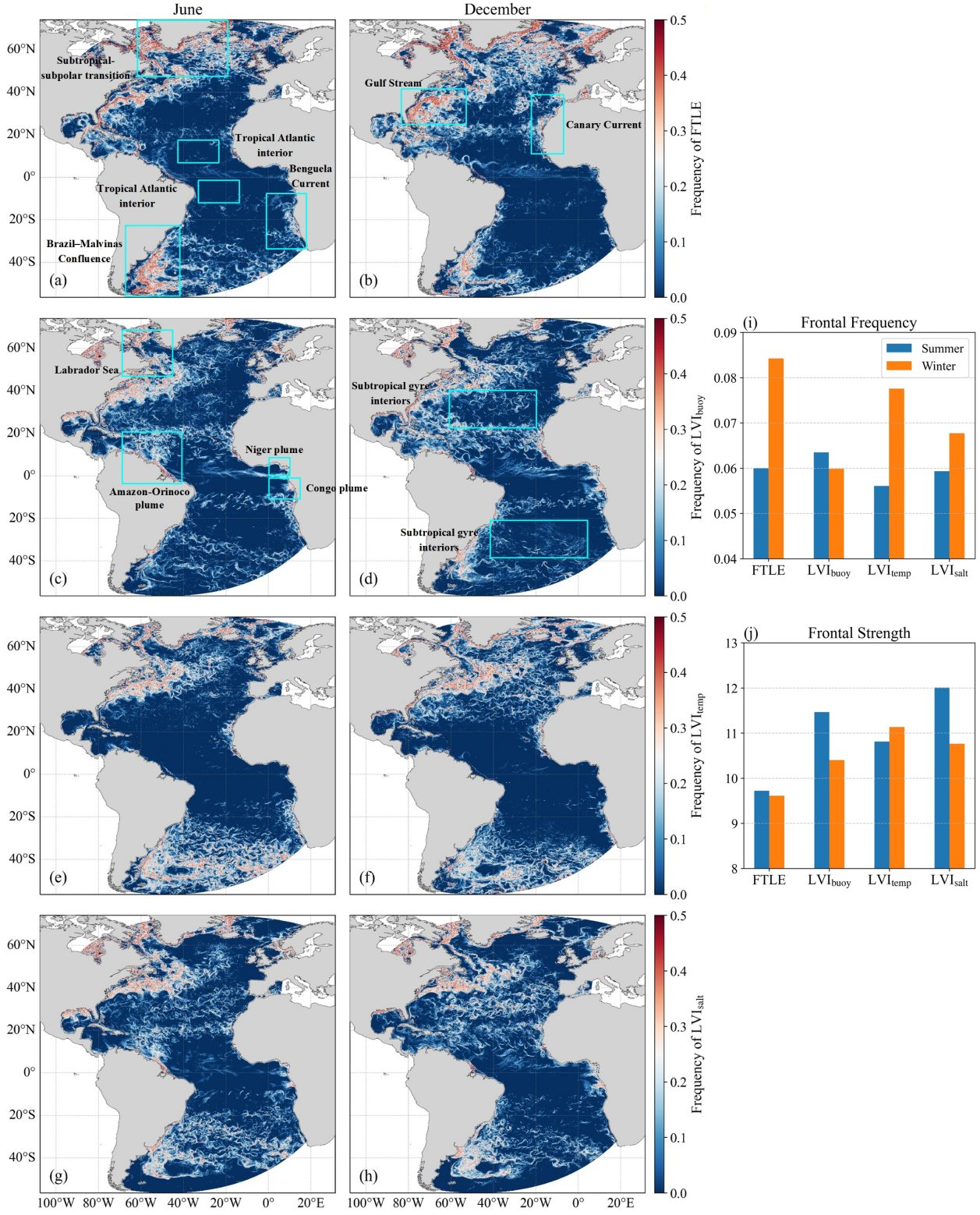

Figure 3. Spatial and seasonal variations of submesoscale fronts in the Atlantic Ocean. (a–h) Spatial distributions of frontal occurrence frequency in the Atlantic Ocean during June and December. Rectangular boxes and text labels indicate the major currents and regions discussed in

the text. Seasonal mean (i) frontal frequency and (j) frontal strength. Blue bars represent summer and orange bars represent winter. Frequency is defined as the ratio of the number of days with detected fronts to the total number of days in each month. Strength is the monthly mean of normalized frontal intensity, a dimensionless quantity.

4 Relationships of dynamical, thermal, and haline fronts to density fronts

Submesoscale fronts develop through frontogenesis, which can be driven by multiple processes, including deformation by mesoscale strain fields and mixed-layer instabilities. In general, density and dynamical fronts represent complementary aspects of submesoscale frontogenesis. Density fronts diagnosed by LVI indicate the sharpening of lateral buoyancy gradients, whereas dynamical fronts diagnosed by backward-time FTLE identify attracting LCSs and deformation zones associated with strong strain and convergence. LVI_{temp} and LVI_{salt} represent subsets of density fronts, depending on whether temperature or salinity dominates the local density variability. However, these indicators may detect fronts that do not correspond to true density fronts, when temperature and salinity gradients compensate each other. FTLE may capture strong strain fields associated with eddies that have weak relative vorticity and do not necessarily correspond to submesoscale fronts (Shcherbina et al., 2013).

In this Section, we quantify the regions and conditions under which density fronts diagnosed by LVI_{buoy} are captured by FTLE, LVI_{temp}, and LVI_{salt}, individually or in combination, as well as the conditions under which these diagnostics produce false detections. We also examine the mechanisms responsible for the different frontal configurations.

4.1 Diagnostic framework

To quantify the relationship among dynamical, thermal, haline and density fronts, we classify the dominant co-occurrence patterns of these fronts relative to density fronts. For each grid point, only occurrences exceeding 1 day were considered. A front is classified as dominant when its frequency exceeds that of the second most frequent front by more than 5 days. In coexistent regions, all fronts with frequencies within 5 days of the maximum are considered simultaneously active, and their combinations were used to define the co-occurrence types. Since dynamical, density, thermal, or haline fronts rarely occur alone, we exclude these isolated categories and consider only types coexistent with density fronts to build the categorical maps (Figures 4, 6, and S20). Percentages were calculated as the fraction of each category area relative to all classified categories area.

In addition, to quantify the relative importance of thermal expansion and haline contraction effects on density, we calculate the horizontal Turner angle:

$$Tu_x = arctan\left(\frac{\alpha T_x}{\beta S_x}\right), \tag{10}$$

where α is the thermal expansion coefficient, β is the haline contraction coefficient, T_x and S_x are the gradients of temperature and salinity in the zonal direction. Based on Tu_x, gradients can be classified in four types: Tu_x in $[-\pi/2, -\pi/4]$ indicates Temperature-controlled Reinforcement (TR); Tu_x in $[-\pi/4, 0]$ indicates Salinity-controlled Reinforcement (SR); Tu_x in $[0, \pi/4]$ indicates Salinity-controlled Compensation (SC); Tu_x in $[\pi/4, \pi/2]$ indicates Temperature-controlled Compensation (TC). The meridional Turner angle (Tu_y), shows a similar spatial distribution (Figure S21).

To characterize how closely each indicator overlaps with density fronts locally, we compute the F1-score within a 201×201 pixel sliding window. The F1-score is mathematically equivalent to the Dice coefficient, a metric often used in segmentation tasks for measuring spatial overlap between two binary maps. In practice, F1-score is defined as the harmonic mean of precision and recall,

$$\text{F1-score} = \frac{2|X \cap Y|}{|X| + |Y|}, \tag{11}$$

which avoids a bias toward under-detection or over-detection. In Equation 11, X denotes the sets of detected fronts (LVI_{temp}, LVI_{salt}, and FTLE) and Y represents the reference density fronts (LVI_{buoy}).

4.2 Widespread density fronts associated with dynamical and thermohaline fronts

The distribution of dominant frontal types shows strong regional contrasts across the Atlantic Ocean (Figure S20). The most widespread co-occurrence patterns are those in which density fronts occur together with FTLE and at least one tracer-based front, namely "All", "FTLE + Temp", and "FTLE + Salt", which together account for 51.5% of all classified category area in Figure S20. These combinations are expected due to the nature of frontogenetic processes.

All four types of fronts are simultaneously active along major boundary currents, including the GS and its extension, the North Atlantic Drift, the Brazil Current, the Canary Current, the Greenland Current, and the Labrador Current (Figures 4a and 4b). These regions also exhibit high F1-scores for all three indicators relative to density fronts (Figure 5). These zones are characterized by intense strain and sharp horizontal thermohaline gradients (Figures S18 and S19), creating favorable conditions for the emergence and interaction of all types of fronts. In the "All" region, SC and TC types each account for ~40%, indicating that density fronts in this region are primarily compensated. For example, the Gulf Stream advects warm, saline water northward and encounters cold, fresh subpolar water, thereby compensating for the density gradient (Figure S19). Compensation does not necessarily imply a weak buoyancy gradient. The buoyancy gradient magnitude

$$|\nabla b| = g|\alpha \nabla T - \beta \nabla S|, \tag{12}$$

can still be substantial when the residual between thermal and haline contributions remains large. Only when the temperature-controlled and salinity-controlled effects are nearly equal (i.e., $Tu_x = \pi/4$), the buoyancy gradient approaches zero, leading to the disappearance of density fronts (Figure 8).

The "FTLE + Temp" category is concentrated in major frontal systems, including the GS, BMC, Benguela Current, and subpolar regions. The local-overlap patterns are consistent with the occurrence distributions (Figure 5). Compared with LVI_{salt}, LVI_{temp} show higher F1-scores in these regions (Figures 5a and 5d), where thermal stratification is the primary contributor to buoyancy gradients (Figures 4c and 4d). At the same time, FTLE also maintains substantial overlap with density fronts in these regions (Figures 5c and 5f), where density fronts are controlled jointly by dynamic deformation and thermal stratification. In winter, the "FTLE + Temp" category becomes more widespread because surface cooling steepens thermal gradients, while stronger strain and frontogenesis enhance tracer convergence and sharpens frontal structures (Brannigan et al., 2015; Prend et al., 2025).

The "FTLE + Salt" category is most prominent in regions influenced by freshwater forcing, including the tropical Atlantic influenced by the Amazon and Congo river plumes, as well as the boundary currents in the subpolar North Atlantic (Figures 4c and 4d). Meanwhile, FTLE and LVI_{salt} have higher F1-scores than LVI_{temp} (Figure 5). In these areas, freshwater inputs from rivers, sea-ice melt, and precipitation generate strong salinity gradients intensified by deformation of the velocity field.

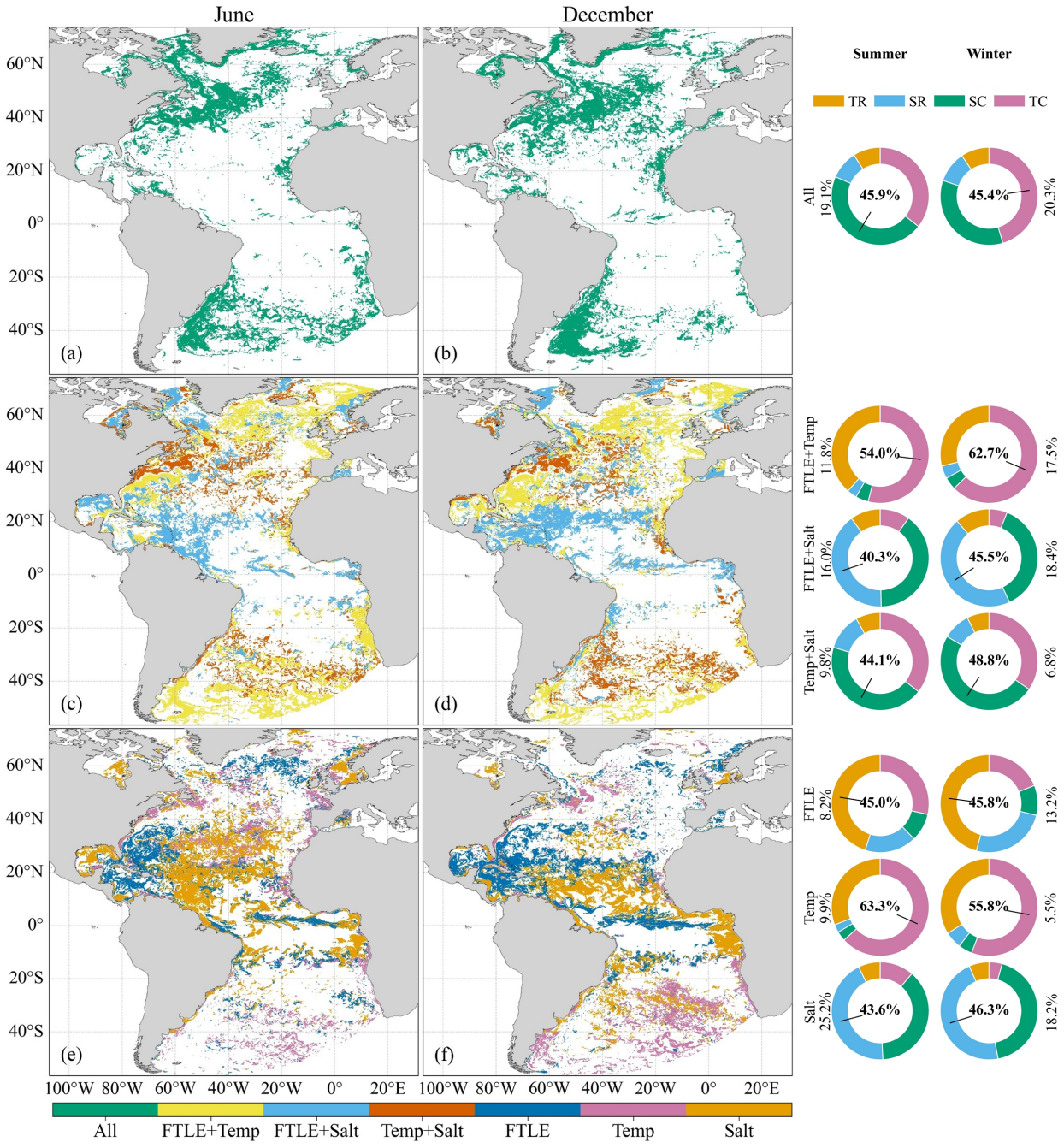

Figure 4. Dominant co-occurrence types of dynamical (FTLE), thermal (LVI_{temp}), and haline fronts (LVI_{salt}) with density fronts (LVI_{buoy}) in June and December. (a, b) show regions where all four

types of fronts are active simultaneously ("All"). (c, d) show two-front combinations with density fronts ("Temp + Salt", "FTLE + Temp", and "FTLE + Salt"). (e, f) show regions where only one type co-occurs with density fronts ("Temp", "Salt", and "FTLE"). Donut charts summarize the percentage distribution of Tu_x categories for each dominant frontal type co-occurring with density fronts in summer and winter. The percentage beside each "donut" indicates the area fraction of the co-occurrence category relative to all density-front occurrences within the corresponding season. Summer is defined as June in the Northern Hemisphere and December in the Southern Hemisphere, and vice versa for winter.

The categorical map of Turner angle in Figure S21 is consistent with the annual-mean large-scale surface Turner angle shown in Figure 3d of Whalen and Drushka (2025), who used the monthly World Ocean Atlas sea surface temperature and salinity (1° resolution). Both studies show salinity-dominant fronts in the Tropical Atlantic (due to the influence of major river plumes) and temperature-dominant fronts in the subtropical Atlantic. Additionally, we find more salinity-controlled compensation in the subtropical Atlantic, a process known to occur at submesoscale (Coadou-Chaventon et al., 2024; Spiro Jaeger & Mahadevan, 2018).

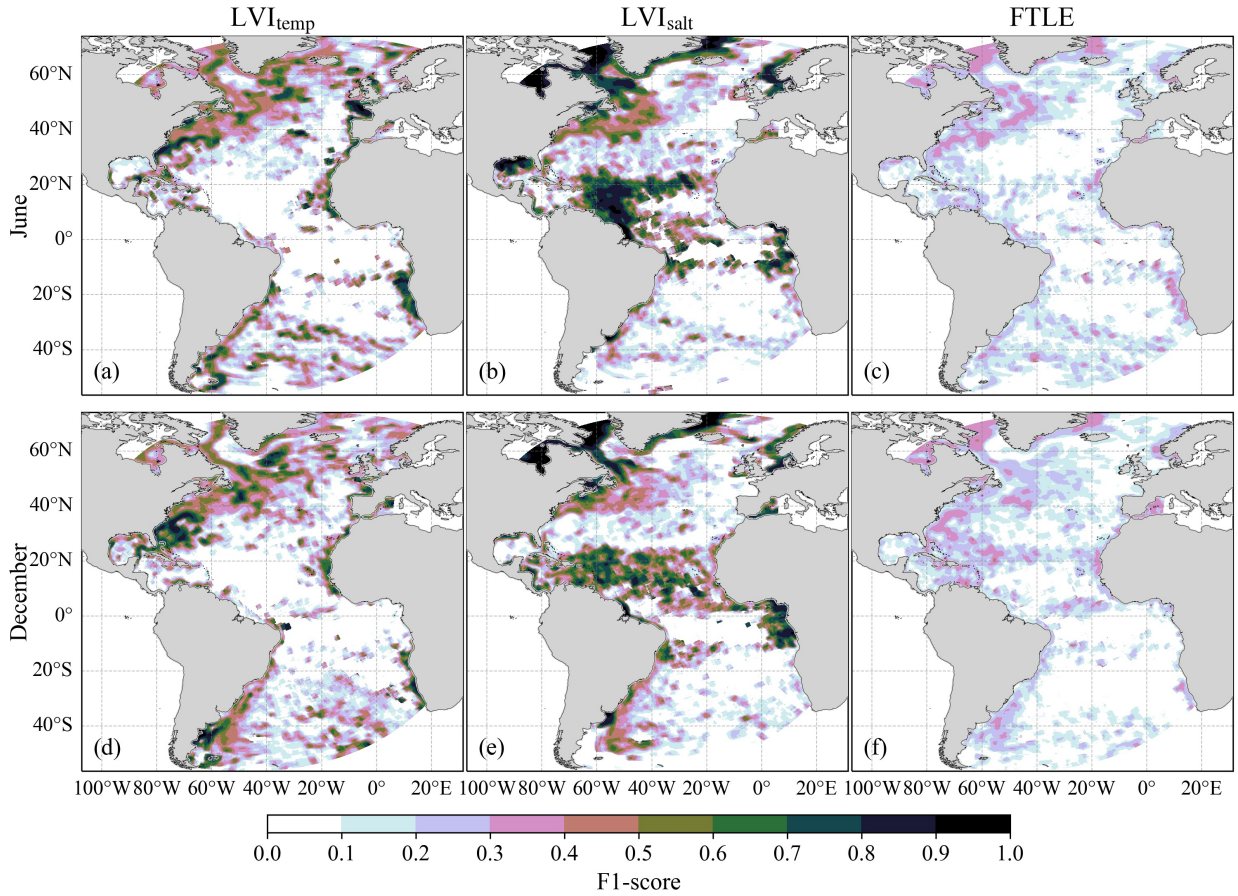

Figure 5. Detection performance of surface submesoscale density fronts in the Atlantic Ocean. (a–c) show the F1-scores of LVI$_{temp}$, LVI$_{salt}$, and FTLE relative to density fronts in June. (d–f) show the same for December.

4.3 Complementary value of FTLE and LVI

The comparison among LVI_{temp}, LVI_{salt}, and FTLE shows that no single diagnostic provides a complete representation of density fronts across the Atlantic (Figures 4e and 4f). Tracer-based LVI is effective when the selected tracer dominates density gradients, but becomes less reliable when density variability is controlled by the other tracer. FTLE reduces this tracer-specific bias. In salinity-dominated regions such as the Amazon plume and the Gulf of Guinea, LVI_{temp} fails to capture density fronts, with F1-scores approaching zero (Figures 5a and 5d). FTLE still achieves moderate F1-scores (Figures 5c and 5f). Similarly, in temperature-dominated regions such as the BMC, Benguela Current, Bay of Biscay, and the subtropical South Atlantic, FTLE clearly outperforms LVI_{salt}. These regional contrasts indicate that FTLE is less constrained by whether density variability is primarily controlled by temperature or salinity.

The regional examples clarify how FTLE complements tracer-based LVI. In the first case, temperature and salinity gradients are weak but reinforce each other, enhancing the density gradient (Figures 7a–e). As a result, density fronts are detected despite the absence of temperature or salinity fronts and align well with FTLE structures. In the second case, strong temperature and salinity fronts are observed; however, their compensating effect weakens the net buoyancy gradient, leading to sparse density fronts (Figures 7f–j). Although both density and dynamical fronts are limited in number, they exhibit greater spatial overlap because they co-locate near major frontal zones. These cases demonstrate FTLE's ability to detect density fronts even in the absence of strong thermohaline gradients, and its insensitivity to thermohaline compensation that may obscure density fronts in Eulerian diagnostics.

The complementary value of FTLE and LVI is further supported by the joint probability density distribution of front intensity and Tu_x (Figure 8). The probability density distributions of LVI_{temp} and LVI_{salt} are concentrated under temperature- and salinity-controlled conditions, respectively (Figures 8c and 8d). In contrast, FTLE is distributed more broadly across different thermohaline regimes (Figure7a). LVI_{temp} and LVI_{salt} show a tendency toward the compensation side, whereas LVI_{buoy} is more strongly skewed toward the reinforcing side (Figure 8b). Furthermore, both FTLE and LVI_{buoy} achieve the highest probabilities at $Tu_x = \pm\pi/2$, corresponding to strong temperature gradients, and at $Tu_x = 0$, corresponding to strong salinity gradients.

The above findings reflect the complementary value of the Lagrangian FTLE flow, which integrates deformation that tends to sharpen existing buoyancy gradients regardless of whether they are controlled primarily by temperature or salinity. Therefore, combining FTLE with Eulerian LVIs can provide more complete and less biased detection of density fronts across contrasting regimes.

4.4 Limitations of front diagnostics

Even with multiple diagnostics, density-front identification requires caution under thermohaline compensation. Near $Tu_x = \pi/4$, the thermal and haline contributions to buoyancy almost cancel each other out (Figure 8b). LVI_{buoy} shows a minimum, while the probability densities of LVI_{temp} and LVI_{salt} remain relatively large. FTLE also exhibits high probabilities of occurrence due to its insensitivity to thermohaline compensation. For example, in Figures 7k–o, density fronts remain sparse because temperature and salinity gradients compensate each other. However, strong velocity shear around eddy boundaries sustains intense stretching, giving rise to prominent FTLE structures.

In addition to the front types that co-occur with density fronts, large parts of the Atlantic are also dominated by co-occurrence types without density fronts (Figure 6). The dominant categories are "Temp + Salt", "FTLE + Temp", and "FTLE + Temp + Salt", accounting for 12.06%, 8.60%, and 7.81% of all classified categories area, respectively. Their broad distributions, particularly in the subpolar North Atlantic and the South Atlantic, indicate that tracer gradients and deformation can coexist even when the instantaneous density-gradient signal is weak or compensated. These results demonstrate that tracer-based or velocity-based diagnostics may over-identify density fronts when used independently, especially under thermohaline compensation.

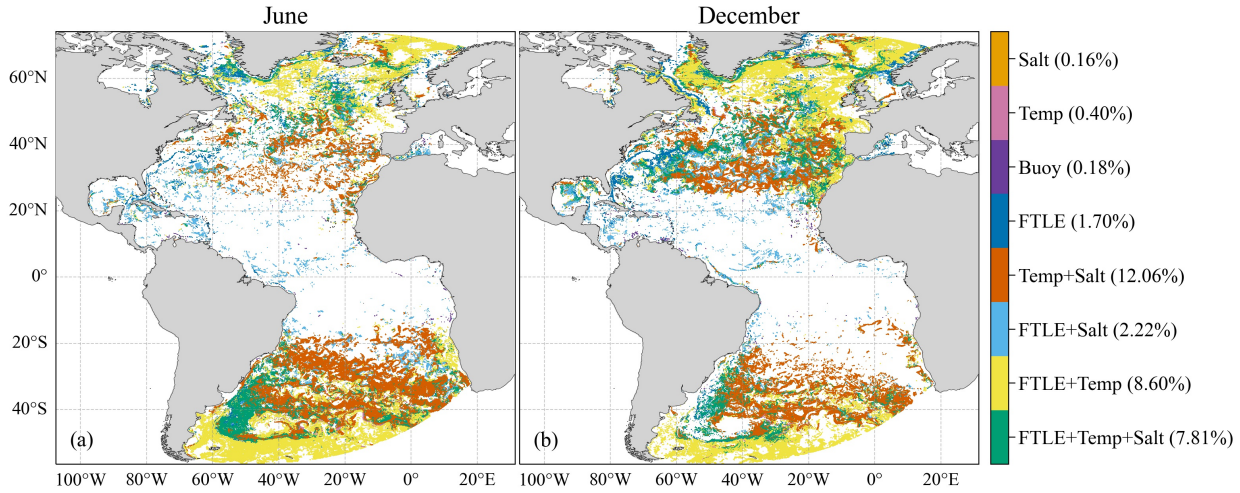

Figure 6. Dominant front types and co-occurrence types without density fronts. "FTLE + Temp + Salt", "FTLE + Temp", "FTLE + Salt", and "Temp + Salt" indicate the simultaneous occurrence of the corresponding front types. "FTLE", "Buoy", "Temp", and "Salt" refer to the most active front types. Percentages for each co-occurrence category are shown in the corresponding panels.

Spatial offset is another limitation of FTLE on density front detection. FTLE integrates deformation along trajectories over a finite interval, whereas LVI_{buoy} is an instantaneous Eulerian measure. As a result, FTLE can highlight regions of accumulated stretching that do not necessarily coincide with the instantaneous maxima of buoyancy gradients, leading to spatial offsets between dynamical and density fronts (Siegelman et al., 2020). Eddy peripheries may also generate stretching and filamentation while vertical relative vorticity or buoyancy gradients remain weak (Shcherbina et al., 2013).

Mismatch can also arise from the way frontal signals are extracted. In our detection framework, submesoscale fronts are identified when the LVI and FTLE fields exceed the 90th-percentile threshold. Therefore, density fronts can remain active due to strong Eulerian tracer gradients even when Lagrangian stretching does not generate an FTLE signal exceeding the threshold used to identify dynamical fronts. These limitations explain why FTLE has lower F1-scores relative to density fronts (Figure 5).

Overall, these results demonstrate that submesoscale density fronts in the Atlantic Ocean arise from the combined effects of Lagrangian dynamical deformation and Eulerian thermohaline gradients. The ability of LVI_{temp} and LVI_{salt} to detect submesoscale density fronts is limited by whether temperature or salinity dominates the local buoyancy gradient. As a result, their performance varies substantially across regions and seasons. In contrast, FTLE is less sensitive to thermohaline effects and provides a more robust detection capability for submesoscale density

fronts across contrasting thermohaline regimes. It is particularly valuable in regions where either temperature or salinity alone provides an incomplete representation of density variability. However, when temperature–salinity compensation severely suppresses density gradients, LVI_{temp}, LVI_{salt}, and FTLE may all show reduced correspondence with density fronts. In general, dynamical and density fronts reflect complementary aspects of frontogenesis, linking the sharpening of lateral density gradients to deformation in the velocity field. Therefore, they are expected to be strongly related, even if they do not perfectly overlap spatially. From a practical detection perspective, the combined use of FTLE and LVI-based methods provides a more comprehensive framework for distinguishing submesoscale density fronts across the Atlantic Ocean.

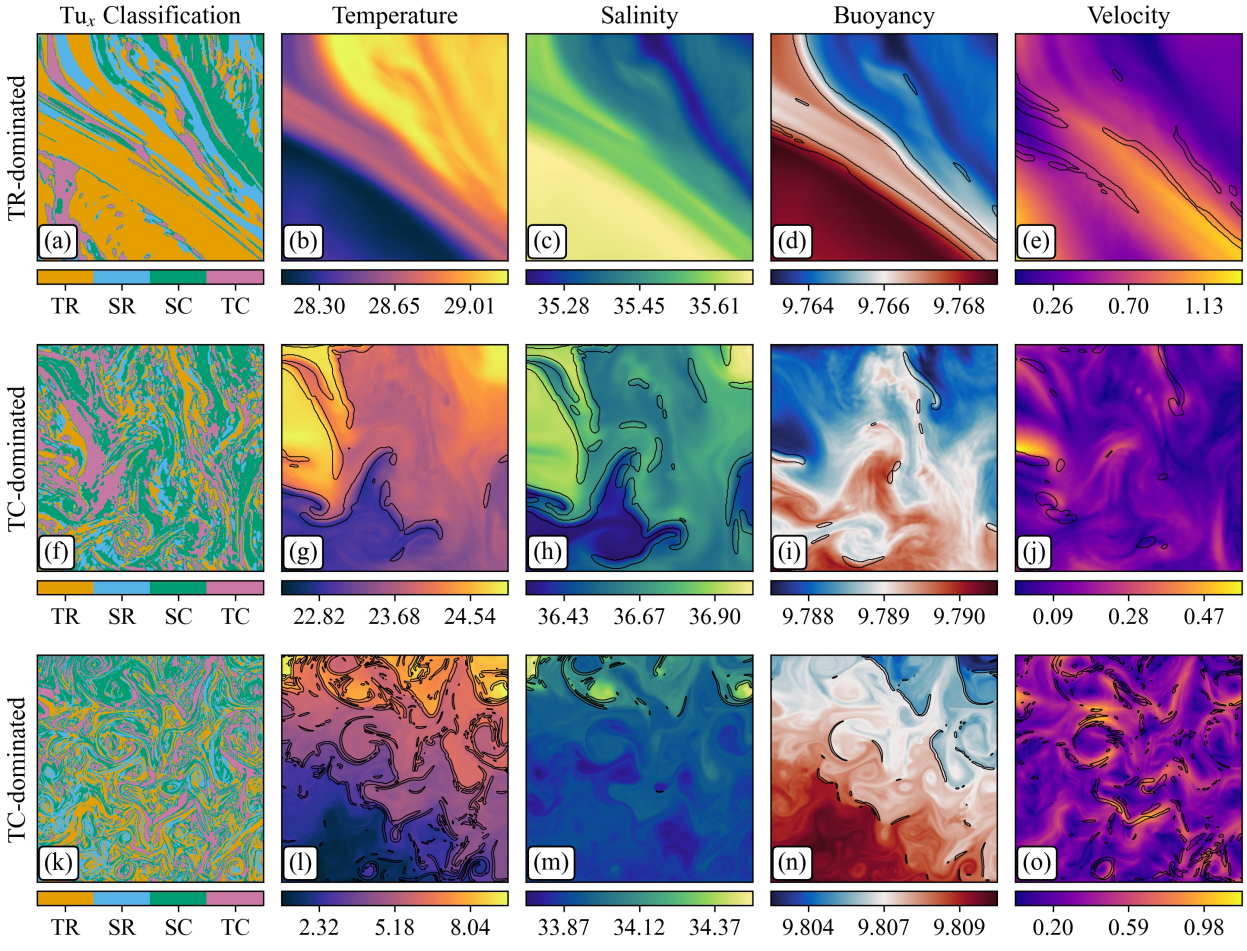

Figure 7. Spatial distribution of Tu_x classifications and corresponding physical fields with frontal indicators. (a), (f), and (k) represent regions of TR, TC, and TC. (b–e), (g–j), and (l–o) present temperature, salinity, buoyancy, and velocity for the same regions, respectively, with contours indicating thermal, haline, density, and dynamical fronts.

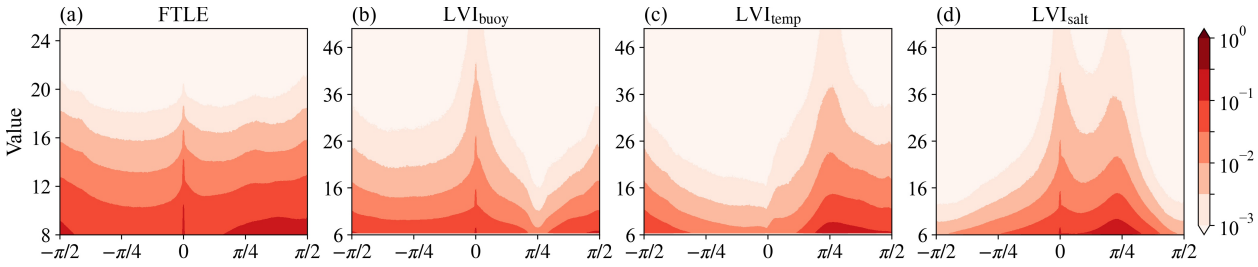

Figure 8. Joint probability density distributions of front intensity and Tu_x for (a) dynamical fronts, (b) density fronts, (c) thermal fronts, and (d) haline fronts. The x-axis represents Tu_x ranging from $-\pi/2$ to $\pi/2$, and the y-axis shows the corresponding frontal intensity. Color shading indicates the probability density on a logarithmic scale.

5 Performance of FTLE derived from the coarse velocity

The above results show that FTLE computed from hourly 1-km velocity can robustly detect density fronts across contrasting thermohaline regimes and is less affected by temperature–salinity compensation than the LVI method. These findings raise a critical question: to what extent can FTLE retain this performance when applied to the much coarser velocity fields available from present-day satellite observations? To address this, we evaluate FTLE computed from coarser geostrophic velocities representative of satellite altimetry. We apply a uniform 12.5 × 12.5 km spatial filter to daily geostrophic velocity fields, matching the resolution used by AVISO FSLE product. Previous studies show that the effective spatial resolution of AVISO velocity fields can exceed 100 km, due to measurement noise and along-track sampling constraints (Ballarotta et al., 2019; Picard et al., 2025). Therefore, we additionally compute FTLE from velocity fields smoothed to a 100-km resolution, representing the lower bound of altimetric resolving capability.

All FTLE computations use δ_0 = 1 km, T = 5 days, and dt = 0.5 days. For the 12.5-km geostrophic velocity case (Figure S22), choosing δ_0 = 1 km preserves mesoscale structures while still revealing fine-scale filaments. These filaments are not numerical artefacts, as their morphological coherence and spatial alignment closely match those obtained from daily 1-km velocities (Figures 9b and 9c). This consistency across resolutions provides confidence that FTLE retains meaningful information even when the underlying flow is coarsened.

FTLE is highly sensitive to the integration time T (Figures S22 d–f and S23 d–f). If T is too short, deformation structures remain underdeveloped; if too long, short-lived fronts are missed (Prants et al., 2014). Fahlbusch et al. (2024) showed that near-surface density variability is dominated by processes on time scales up to ~10 days, so we evaluate FTLE over this range and calculate the F1 score between FTLE-derived fronts and LVI buoy fronts (Figure S24). For the 12.5-km velocity fields, the F1 score peaks at T = 3 days and then decreases steadily as T increases, indicating that excessive integration tends to smear or displace fine-scale fronts. For the 100-km velocity fields, the F1 score increases gradually and reaches a maximum at T = 7 days, reflecting the slower evolution of fronts at coarser resolution. Considering both resolutions, an integration time of 5 days provides a balanced performance, maintaining relatively high F1 scores for both cases. Additionally, we use dt = 0.5 day, which avoids numerical artefacts arising from coarse steps (e.g., dt = 1 day; Figure S22i) while remaining computationally efficient. We do not smooth the FTLE fields using an 11×11 mean filter because the underlying velocity field already has a coarse resolution, and with a 5-day integration the FTLE derived from daily 12.5-km or 100-km velocities does not resolve the same fine-scale structures produced by FTLE computed from hourly, 1-km velocities. Instead, we apply the same masking strategy to the FTLE fields to extract the dynamical fronts, which is described in Section 2.4.

As expected, increasing the temporal and spatial resolution of the velocity field progressively reveals sharper and more filamentary LCS signatures (Figures 9a–9d). As geostrophic velocity is divergence-free, FTLE cannot directly identify any Eulerian convergence zones. However, by comparing with FTLE derived from the full velocity smoothed to the same resolution, we find a high similarity with FTLE derived from geostrophic velocity (Figures 9e–9h). Moreover, as the velocity field becomes coarser, the structures captured by the two FTLE become more identical (Figures 9a–9c and 9e–9g). These findings imply that in nondivergent flows (geostrophic velocity or sufficiently coarse velocity), frontogenesis is associated with kinematic criteria other than divergence. As argued by Hetland et al. (2025), when the flow is primarily nondivergent ($\delta \approx 0$), frontal maintenance can be dominated by the effective (normal)

strain in a frontal coordinate system. In that case, fronts strengthen through cross-front contraction and along-front divergence ($\tilde{u}_x \approx -\tilde{v}_y$), also called confluent contraction (see Figure 10 in Hetland et al., 2025). Such kinematics organize coherent attracting/stretching LCS, yielding FTLE ridges aligned with fronts even in the absence of explicit horizontal convergence. Conversely, as the fields are resolved at 1-km and hourly resolution (Figures 9d and 9h), the role of divergence in frontogenesis becomes increasingly important. Deformation in the hourly, 1-km geostrophic flow is strongly modulated by high-frequency oscillations, making it difficult for a coherent, cumulatively effective net contraction to persist over the finite integration period and thereby smearing attracting FTLE ridges. By contrast, the full flow includes ageostrophic cross-front circulations that provide a more sustained net contraction, making the LCS structures in Figure 9h noticeably sharper and more coherent. More generally, the submesoscale full flow permits substantial horizontal convergence, allowing FTLE to capture more explicit convergence signatures. Overall, these results indicate that FTLE can diagnose frontal LCS through strain-dominated frontogenesis in nondivergent geostrophic flows.

Consistent with the structural refinement, the mean F1-scores increase from 0.13 for the 100-km full velocity field to 0.18 for the 12.5-km field and 0.21 for the 1-km field. The small difference between the 1-km and 12.5-km results indicates that FTLE retains useful diagnostic skill for detecting submesoscale density fronts even when derived from coarse-resolution velocity. For geostrophic flow, the mean F1-scores of 100-km and 12.5-km fields are 0.13 and 0.16, respectively. At the 12.5-km scale, the skill of FTLE in identifying density fronts is partly limited when computed from the geostrophic flow, because the geostrophic component lacks convergence that sharpens density fronts. In contrast, at the 100-km scale both the full and geostrophic flows are nearly non-divergent and dominated by large-scale balanced dynamics, leading to similarly low F1 scores. At this extreme level of smoothing, only dynamically energetic regions retain detectible FTLE ridges, such as western boundary currents, equatorial jets, and the South Atlantic westerly wind belt (Figures 10b and 10d). This finding reflects the fact that strong background shear and strain in these regions can survive heavy smoothing, whereas weaker submesoscale features cannot.

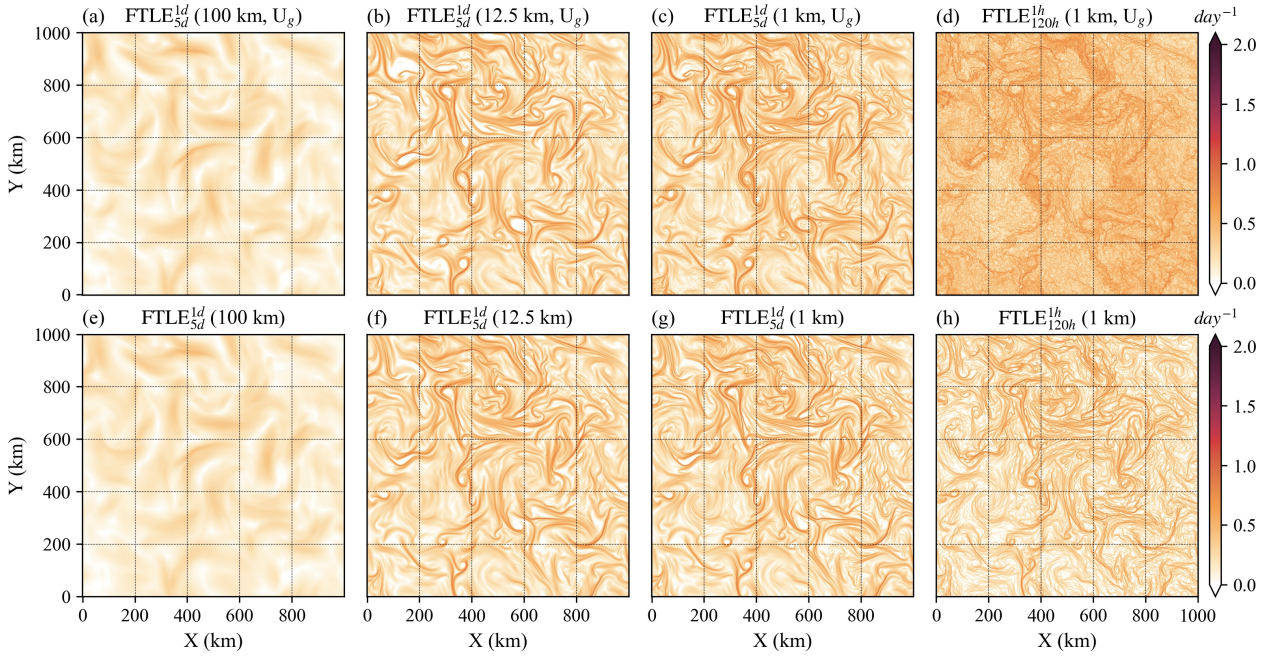

Figure 9. FTLE computed in a North Atlantic subregion using geostrophic (top row) and full (bottom row) velocity fields at different spatial and temporal resolutions. (a) FTLE derived from daily geostrophic velocity fields that were uniformly filtered to 100 km × 100 km (T = 5 days, dt = 0.5 days). (b) FTLE derived from daily geostrophic velocity fields that were uniformly filtered to 12.5 km × 12.5 km (T = 5 days, dt = 0.5 days). (c) FTLE derived from daily 1-km geostrophic velocity fields (T = 5 days, dt = 0.5 days). (d) FTLE derived from hourly 1-km geostrophic velocity fields (T = 120h, dt = 12h). (e–h) same as (a–d) but using full velocity fields. All FTLE fields use an initial separation δ_0 = 1 km.

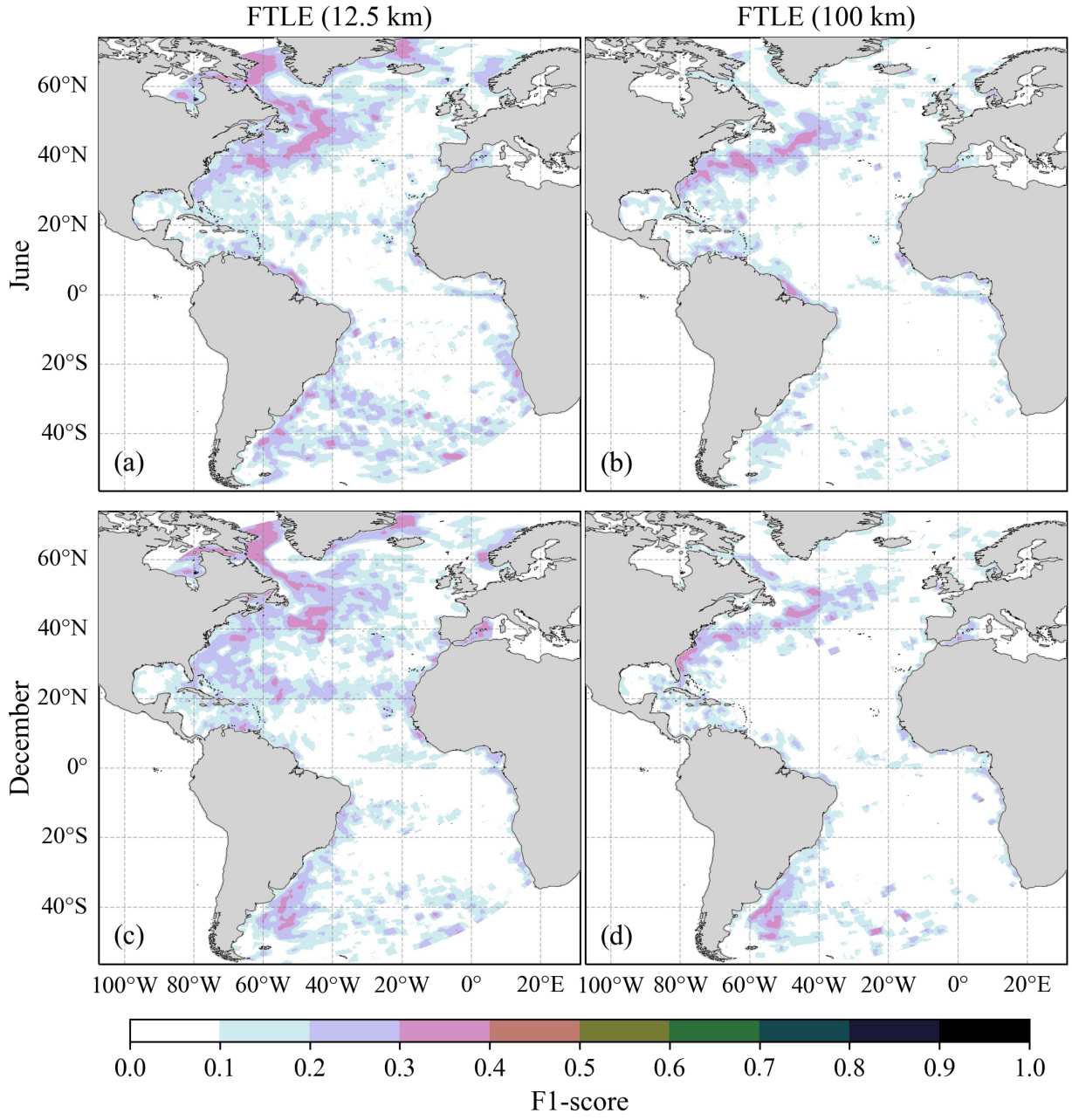

Figure 10. FTLE detection performance based on geostrophic velocities at different resolutions in June and December. The F1-scores shown here are computed between density fronts (LVI_{buoy}) and dynamical fronts (FTLE). (a, c) F1-scores for FTLE computed from the daily 12.5-km velocity fields. (b, d) F1-scores for FTLE computed from the daily 100-km velocity fields.

6 Conclusions

In this study, we use a high-resolution, submesoscale permitting simulation of the Atlantic Ocean (GIGATL1) to investigate the detection and dynamics of surface submesoscale fronts. We apply two complementary diagnostics: the Eulerian LVI, which captures thermal, haline, and

density fronts based on the variability of surface tracers, and the Lagrangian FTLE, which identifies dynamically active regions associated with stretching and tracer convergence. By implementing scale-selective temporal and spatial filtering, and a consistent thresholding approach, we extract frontal features at scales of 1–10 km and 1–10 days, and compare their dynamical characteristic and spatial distributions. We further examine how dynamical, thermal, and haline fronts relate to density fronts and assess the potential of FTLE and temperature-based LVI as indicators for density-front detection.

The detected dynamical and density fronts exhibit the strongest submesoscale signatures, indicating their closer connection to deformation-driven frontogenesis and ageostrophic secondary circulation. Submesoscale fronts exhibit a clear asymmetry toward cyclonic vorticity and convergence, resulting from the asymmetric response of the vorticity tendency to vortex stretching. These findings are consistent with previous studies and support the validity of our submesoscale front detection approach.

Spatial and seasonal patterns of frontal activity across the Atlantic indicate that dynamical fronts are both widespread and persistent. Their frequency increases during winter, primarily due to intensified frontal dynamics, including elevated strain rate and vorticity. Thermohaline fronts exhibit greater regional and seasonal variability. Thermal fronts are more active in winter as a result of surface cooling, whereas haline fronts reach peak activity in summer near major river outflows, including the Amazon and Congo. Density fronts, influenced by either temperature- or salinity-controlled effects, exhibit a broader distribution and combine the characteristics of both thermal and haline fronts. In tropical and subtropical gyres, thermohaline compensation frequently reduces density gradients. This process leads to sparse density fronts, even when dynamical activity persists.

The co-occurrence of density fronts with FTLE and at least one tracer-based front indicates that deformation-driven frontogenesis commonly sharpens pre-existing thermal or haline gradients, thereby producing density fronts with both dynamical and thermohaline signatures. The comparison among LVI_{temp}, LVI_{salt}, and FTLE reveals their complementary roles in density-front detection. LVI_{temp} and LVI_{salt} are effective when density variability is dominated by temperature or salinity, respectively, but they may become less reliable when the other tracer controls the buoyancy gradient. In compensated regions, LVI_{temp} and LVI_{salt}-based fronts may produce false positives, whereas in reinforced regions, they may miss density fronts. In contrast, FTLE is less sensitive to thermohaline effects, allowing it to identify density fronts across contrasting thermohaline regimes. Nevertheless, FTLE can identify stretching structures that do not coincide with instantaneous buoyancy gradients, and may also cause false detection of density fronts when thermohaline compensation suppresses the density signal.

The methodology developed here can be applied to observational datasets, especially those combining high-resolution satellite-derived SST and surface velocities. Unfortunately, satellite SSS observations do not resolve submesoscale features (Boutin et al., 2018), but FTLE may partially compensate that and provide information about density fronts in salinity dominated regions. However, care must be taken when interpreting FTLE structures without direct density observations, as tracer compensation may obscure density fronts. In addition, our results indicate that while FTLE retains meaningful skill at mesoscale-resolving resolutions (e.g., 12.5 km), its performance diminishes at altimetry scales approaching ~100 km, where only the strongest deformation features remain detectable. This behavior reflects the dependence of FTLE on the resolved strain–rate variability, emphasizing the importance of velocity resolution when applying

FTLE to observational products. As higher-resolution surface velocity products from the Surface Water and Ocean Topography (SWOT) mission become available, FTLE-based diagnostics are expected to better resolve submesoscale frontal structures. Future work should consider integrating additional satellite variables such as ocean color, and using machine learning to classify frontal zones based on a combination of the different diagnostics presented here, as well as information on the vertical density profiles (Yao et al., 2025; Yao & Taylor, 2026). Further improvements may include adaptive thresholding for different dynamic regions and incorporating vertical data from model reanalysis or autonomous observations. Overall, this study establishes a benchmark framework for interpreting submesoscale frontal dynamics and guides the design of observational strategies to resolve fine-scale ocean processes.

CRediT authorship contribution statement

Qian Liu: Conceptualization, Methodology, Software, Validation, Formal analysis, Data Curation, Writing – Original Draft, Writing – Review & Editing, Visualization. **Dante C. Napolitano:** Investigation, Methodology, Writing – Original Draft, Writing – Review & Editing, Visualization, Supervision. **Jonathan Gula:** Investigation, Methodology, Conceptualization, Resources, Data Curation, Writing – Original Draft, Writing – Review & Editing, Supervision, Project administration. **Mengjiao Wang:** Writing – Review & Editing. **Yingjie Liu:** Writing – Review & Editing. **Le Gao:** Writing – Review & Editing. **Xiaofeng Li:** Conceptualization, Resources, Writing – Review & Editing, Supervision, Project administration, Funding acquisition.

Declaration of competing interest

The authors declare that they have no known competing financial interests or personal relationships that could have appeared to influence the work reported in this paper.

Acknowledgments

This study was supported by the National Natural Science Foundation of China (42306194, 42376175), Self-Deployed Project of the Institute of Oceanology, Chinese Academy of Sciences (IOCASZZZX103), National Natural Science Foundation of China (42221005), National Key R&D Program of China (2022YFE0204600), Qingdao Science and Technology for People's Livelihood Demonstration Special Project (25-1-5-cspz-18-nsh), China Scholarship Council, and by the French National Agency for Research (ANR) through the project DEEPER (ANR-19-CE01-0002-01). Simulations were performed using HPC resources from GENCI-TGCC (2024-A0170112051), and from HPC facilities DATARMOR of "Pôle de Calcul Intensif pour la Mer" at Ifremer, Brest, France. The authors would like to express their gratitude to the reviewers for their helpful and constructive feedback.

Data availability

The information about the GIGATL1 can be found at https://doi.org/10.5281/zenodo.4948523. AVISO FSLE product can be found at: https://doi.org/10.24400/527896/A01-2022.002.

References

Adams, K. A., Hosegood, P., Taylor, J. R., Sallée, J.-B., Bachman, S., Torres, R., et al. (2017). Frontal Circulation and Submesoscale Variability during the Formation of a Southern Ocean Mesoscale Eddy. J. Phys. Oceanogr., 47(7), 1737-1753. https://doi.org/https://doi.org/10.1175/JPO-D-16-0266.1

867 Allshouse, M. R., & Peacock, T. (2015a). Lagrangian based methods for coherent structure detection. Chaos: An
868 Interdisciplinary Journal of Nonlinear Science, 25(9), 097617. https://doi.org/10.1063/1.4922968
869 Allshouse, M. R., & Peacock, T. (2015b). Refining finite-time Lyapunov exponent ridges and the challenges of
870 classifying them. Chaos: An Interdisciplinary Journal of Nonlinear Science, 25(8), 087410.
871 https://doi.org/10.1063/1.4928210
872 Aravind, H. M., Verma, V., Sarkar, S., Freilich, M. A., Mahadevan, A., Haley, P. J., et al. (2023). Lagrangian
873 surface signatures reveal upper-ocean vertical displacement conduits near oceanic density fronts. Ocean
874 Modell., 181, 102136. https://doi.org/https://doi.org/10.1016/j.ocemod.2022.102136
875 Archer, M. R., Shay, L. K., Jaimes, B., & Martinez-Pedraja, J. (2015). Chapter 11 - Observing Frontal Instabilities
876 of the Florida Current Using High Frequency Radar. In Y. Liu, H. Kerkering, & R. H. Weisberg (Eds.),
877 Coastal Ocean Observing Systems (pp. 179-208). Academic Press.
878 https://doi.org/https://doi.org/10.1016/B978-0-12-802022-7.00011-0
879 Bakun, A. (1990). Global Climate Change and Intensification of Coastal Ocean Upwelling. Science, 247(4939),
880 198-201. https://doi.org/10.1126/science.247.4939.198
881 Ballarotta, M., Ubelmann, C., Pujol, M. I., Taburet, G., Fournier, F., Legeais, J. F., et al. (2019). On the resolutions
882 of ocean altimetry maps. Ocean Sci., 15(4), 1091-1109. https://doi.org/10.5194/os-15-1091-2019
883 Balwada, D., Xiao, Q., Smith, S., Abernathey, R., & Gray, A. R. (2021). Vertical Fluxes Conditioned on Vorticity
884 and Strain Reveal Submesoscale Ventilation. J. Phys. Oceanogr., 51(9), 2883-2901.
885 https://doi.org/https://doi.org/10.1175/JPO-D-21-0016.1
886 Barceló-Llull, B., Drushka, K., & Gaube, P. (2021). Lagrangian Reconstruction to Extract Small-Scale Salinity
887 Variability From SMAP Observations. J. Geophys. Res.: Oceans, 126(3), e2020JC016477.
888 https://doi.org/https://doi.org/10.1029/2020JC016477
889 Barkan, R., Molemaker, M. J., Srinivasan, K., McWilliams, J. C., & D'Asaro, E. A. (2019). The Role of Horizontal
890 Divergence in Submesoscale Frontogenesis. J. Phys. Oceanogr., 49(6), 1593-1618.
891 https://doi.org/https://doi.org/10.1175/JPO-D-18-0162.1
892 Becker, J. J., Sandwell, D. T., Smith, W. H. F., Braud, J., Binder, B., Depner, J., et al. (2009). Global Bathymetry
893 and Elevation Data at 30 Arc Seconds Resolution: SRTM30_PLUS. Mar. Geod., 32(4), 355-371.
894 https://doi.org/10.1080/01490410903297766
895 Boccaletti, G., Ferrari, R., & Fox-Kemper, B. (2007). Mixed Layer Instabilities and Restratification. J. Phys.
896 Oceanogr., 37(9), 2228-2250. https://doi.org/https://doi.org/10.1175/JPO3101.1
897 Boffetta, G., Lacorata, G., Redaelli, G., & Vulpiani, A. (2001). Detecting barriers to transport: a review of different
898 techniques. Physica D, 159(1), 58-70. https://doi.org/https://doi.org/10.1016/S0167-2789(01)00330-X
899 Boutin, J., Vergely, J. L., Marchand, S., D'Amico, F., Hasson, A., Kolodziejczyk, N., et al. (2018). New SMOS Sea
900 Surface Salinity with reduced systematic errors and improved variability. Remote Sens. Environ., 214, 115-
901 134. https://doi.org/https://doi.org/10.1016/j.rse.2018.05.022
902 Brannigan, L., Marshall, D. P., Naveira-Garabato, A., & George Nurser, A. J. (2015). The seasonal cycle of
903 submesoscale flows. Ocean Modell., 92, 69-84.
904 https://doi.org/https://doi.org/10.1016/j.ocemod.2015.05.002
905 Calil, P. H. R., & Richards, K. J. (2010). Transient upwelling hot spots in the oligotrophic North Pacific. J.
906 Geophys. Res.: Oceans, 115(C2). https://doi.org/https://doi.org/10.1029/2009JC005360
907 Callies, J., Ferrari, R., Klymak, J. M., & Gula, J. (2015). Seasonality in submesoscale turbulence. Nat. Commun.,
908 6(1), 6862. https://doi.org/10.1038/ncomms7862
909 Canuto, V. M., Howard, A., Cheng, Y., & Dubovikov, M. S. (2001). Ocean Turbulence. Part I: One-Point Closure
910 Model—Momentum and Heat Vertical Diffusivities. J. Phys. Oceanogr., 31(6), 1413-1426.
911 https://doi.org/https://doi.org/10.1175/1520-0485(2001)031<1413:OTPIOP>2.0.CO;2
912 Capet, X., McWilliams, J. C., Molemaker, M. J., & Shchepetkin, A. F. (2008). Mesoscale to Submesoscale
913 Transition in the California Current System. Part I: Flow Structure, Eddy Flux, and Observational Tests. J.
914 Phys. Oceanogr., 38(1), 29-43. https://doi.org/https://doi.org/10.1175/2007JPO3671.1
915 Carton, J. A., & Giese, B. S. (2008). A Reanalysis of Ocean Climate Using Simple Ocean Data Assimilation
916 (SODA). Mon. Weather Rev., 136(8), 2999-3017. https://doi.org/https://doi.org/10.1175/2007MWR1978.1
917 Chavez, F. P., & Messié, M. (2009). A comparison of Eastern Boundary Upwelling Ecosystems. Prog. Oceanogr.,
918 83(1), 80-96. https://doi.org/https://doi.org/10.1016/j.pocean.2009.07.032
919 Chelton, D. B., Schlax, M. G., & Samelson, R. M. (2011). Global observations of nonlinear mesoscale eddies. Prog.
920 Oceanogr., 91(2), 167-216. https://doi.org/https://doi.org/10.1016/j.pocean.2011.01.002

Coadou-Chaventon, S., Speich, S., Zhang, D., Rocha, C. B., & Swart, S. (2024). Oceanic Fronts Driven by the Amazon Freshwater Plume and Their Thermohaline Compensation at the Submesoscale. J. Geophys. Res.: Oceans, 129(7), e2024JC021326. https://doi.org/https://doi.org/10.1029/2024JC021326

Cotté, C., d'Ovidio, F., Dragon, A.-C., Guinet, C., & Lévy, M. (2015). Flexible preference of southern elephant seals for distinct mesoscale features within the Antarctic Circumpolar Current. Prog. Oceanogr., 131, 46-58. https://doi.org/https://doi.org/10.1016/j.pocean.2014.11.011

d'Ovidio, F., Fernández, V., Hernández-García, E., & López, C. (2004). Mixing structures in the Mediterranean Sea from finite-size Lyapunov exponents. Geophys. Res. Lett., 31(17). https://doi.org/https://doi.org/10.1029/2004GL020328

D'Asaro, E., Lee, C., Rainville, L., Harcourt, R., & Thomas, L. (2011). Enhanced Turbulence and Energy Dissipation at Ocean Fronts. Science, 332(6027), 318-322. https://doi.org/10.1126/science.1201515

d'Ovidio, F., Isern-Fontanet, J., López, C., Hernández-García, E., & García-Ladona, E. (2009). Comparison between Eulerian diagnostics and finite-size Lyapunov exponents computed from altimetry in the Algerian basin. Deep Sea Res. Part I, 56(1), 15-31. https://doi.org/https://doi.org/10.1016/j.dsr.2008.07.014

Dave, A. C., & Lozier, M. S. (2010). Local stratification control of marine productivity in the subtropical North Pacific. J. Geophys. Res.: Oceans, 115(C12). https://doi.org/https://doi.org/10.1029/2010JC006507

de Marez, C., Vives, C. R., Portela, E., & Ruiz-Angulo, A. (2025). Mesoscale Ocean Processes: The Critical Role of Stratification in the Icelandic Region. J. Geophys. Res.: Oceans, 130(6), e2025JC022664. https://doi.org/https://doi.org/10.1029/2025JC022664

Duan, W., Cheng, X., Zhou, Y., & Gula, J. (2024). Characteristics of Submesoscale Compensated/Reinforced Fronts in the Northern Bay of Bengal. J. Geophys. Res.: Oceans, 129(10), e2024JC021204. https://doi.org/https://doi.org/10.1029/2024JC021204

Fahlbusch, J. A., Cade, D. E., Hazen, E. L., Elliott, M. L., Saenz, B. T., Goldbogen, J. A., et al. (2024). Submesoscale coupling of krill and whales revealed by aggregative Lagrangian coherent structures. Proceedings of the Royal Society B: Biological Sciences, 291(2017), 20232461. https://doi.org/10.1098/rspb.2023.2461

Fang, L., Balasuriya, S., & Ouellette, N. T. (2020). Disentangling resolution, precision, and inherent stochasticity in nonlinear systems. Phys. Rev. Res., 2(2), 023343. https://doi.org/10.1103/PhysRevResearch.2.023343

Freilich, M. A., Flierl, G., & Mahadevan, A. (2022). Diversity of Growth Rates Maximizes Phytoplankton Productivity in an Eddying Ocean. Geophys. Res. Lett., 49(3), e2021GL096180. https://doi.org/https://doi.org/10.1029/2021GL096180

Gaube, P., Chelton, D. B., Samelson, R. M., Schlax, M. G., & O'Neill, L. W. (2015). Satellite Observations of Mesoscale Eddy-Induced Ekman Pumping. J. Phys. Oceanogr., 45(1), 104-132. https://doi.org/10.1175/jpo-d-14-0032.1

Gough, M. K., Reniers, A., Olascoaga, M. J., Haus, B. K., MacMahan, J., Paduan, J., et al. (2016). Lagrangian Coherent Structures in a coastal upwelling environment. Cont. Shelf Res., 128, 36-50. https://doi.org/https://doi.org/10.1016/j.csr.2016.09.007

Gula, J., Molemaker, M. J., & McWilliams, J. C. (2014). Submesoscale Cold Filaments in the Gulf Stream. J. Phys. Oceanogr., 44(10), 2617-2643. https://doi.org/https://doi.org/10.1175/JPO-D-14-0029.1

Gula, J., Taylor, J., Shcherbina, A., & Mahadevan, A. (2022). Chapter 8 - Submesoscale processes and mixing. In M. Meredith & A. Naveira Garabato (Eds.), Ocean Mixing (pp. 181-214). Elsevier. https://doi.org/https://doi.org/10.1016/B978-0-12-821512-8.00015-3

Gula, J., Theetten, S., Cambon, G., & Roullet, G. (2021). Description of the GIGATL simulations (v1.1). https://doi.org/10.5281/zenodo.4948523

Günther, T., Kuhn, A., & Theisel, H. (2016). MCFTLE: Monte Carlo Rendering of Finite-Time Lyapunov Exponent Fields. Comput. Graphics Forum, 35(3), 381-390. https://doi.org/https://doi.org/10.1111/cgf.12914

Guo, M., Xiu, P., Chai, F., & Xue, H. (2019). Mesoscale and Submesoscale Contributions to High Sea Surface Chlorophyll in Subtropical Gyres. Geophys. Res. Lett., 46(22), 13217-13226. https://doi.org/https://doi.org/10.1029/2019GL085278

Hadjighasem, A., Farazmand, M., Blazevski, D., Froyland, G., & Haller, G. (2017). A critical comparison of Lagrangian methods for coherent structure detection. Chaos: An Interdisciplinary Journal of Nonlinear Science, 27(5), 053104. https://doi.org/10.1063/1.4982720

Haëck, C., Lévy, M., Mangolte, I., & Bopp, L. (2023). Satellite data reveal earlier and stronger phytoplankton blooms over fronts in the Gulf Stream region. Biogeosciences, 20(9), 1741-1758. https://doi.org/10.5194/bg-20-1741-2023

Haller, G. (2015). Lagrangian Coherent Structures. Annu. Rev. Fluid Mech., 47(Volume 47, 2015), 137-162. https://doi.org/https://doi.org/10.1146/annurev-fluid-010313-141322

Haller, G. (2023). Transport Barriers and Coherent Structures in Flow Data. Cambridge University Press.

Hernández-Carrasco, I., López, C., Hernández-García, E., & Turiel, A. (2011). How reliable are finite-size Lyapunov exponents for the assessment of ocean dynamics? Ocean Modell., 36(3), 208-218. https://doi.org/https://doi.org/10.1016/j.ocemod.2010.12.006

Hetland, R. D., Qu, L., & Hinson, K. E. (2025). Frontal Maintenance in Submesoscale Flows. J. Phys. Oceanogr., 55(2), 175-190. https://doi.org/https://doi.org/10.1175/JPO-D-24-0060.1

Hoskins, B. J. (1982). The Mathematical Theory of Frontogenesis. Annu. Rev. Fluid Mech., 14(Volume 14, 1982), 131-151. https://doi.org/https://doi.org/10.1146/annurev.fl.14.010182.001023

Huntley, H. S., Lipphardt Jr, B. L., & Kirwan Jr, A. D. (2011). Surface Drift Predictions of the Deepwater Horizon Spill: The Lagrangian Perspective. In Monitoring and Modeling the Deepwater Horizon Oil Spill: A Record‐Breaking Enterprise (pp. 179-195). https://doi.org/https://doi.org/10.1029/2011GM001097

Karrasch, D., & Haller, G. (2013). Do Finite-Size Lyapunov Exponents detect coherent structures? Chaos: An Interdisciplinary Journal of Nonlinear Science, 23(4), 043126. https://doi.org/10.1063/1.4837075

Klein, P., & Lapeyre, G. (2009). The Oceanic Vertical Pump Induced by Mesoscale and Submesoscale Turbulence. Annu. Rev. Mar. Science, 1(1), 351-375. https://doi.org/10.1146/annurev.marine.010908.163704

Lapeyre, G. (2002). Characterization of finite-time Lyapunov exponents and vectors in two-dimensional turbulence. Chaos: An Interdisciplinary Journal of Nonlinear Science, 12(3), 688-698. https://doi.org/10.1063/1.1499395

Large, W. G., & Yeager, S. G. (2009). The global climatology of an interannually varying air–sea flux data set. Clim. Dyn., 33(2), 341-364. https://doi.org/10.1007/s00382-008-0441-3

Lehahn, Y., d'Ovidio, F., Lévy, M., & Heifetz, E. (2007). Stirring of the northeast Atlantic spring bloom: A Lagrangian analysis based on multisatellite data. J. Geophys. Res.: Oceans, 112(C8). https://doi.org/https://doi.org/10.1029/2006JC003927

Lévy, M., Couespel, D., Haëck, C., Keerthi, M. G., Mangolte, I., & Prend, C. J. (2023). The Impact of Fine-Scale Currents on Biogeochemical Cycles in a Changing Ocean. Annu. Rev. Mar. Science. https://doi.org/10.1146/annurev-marine-020723-020531

Lévy, M., Franks, P. J. S., & Smith, K. S. (2018). The role of submesoscale currents in structuring marine ecosystems. Nat. Commun., 9(1), 4758. https://doi.org/10.1038/s41467-018-07059-3

Liu, Q., Liu, Y., & Li, X. (2023). Characteristics of surface physical and biogeochemical parameters within mesoscale eddies in the Southern Ocean. Biogeosciences, 20(23), 4857-4874. https://doi.org/10.5194/bg-20-4857-2023

Liu, X., & Levine, N. M. (2016). Enhancement of phytoplankton chlorophyll by submesoscale frontal dynamics in the North Pacific Subtropical Gyre. Geophys. Res. Lett., 43(4), 1651-1659. https://doi.org/https://doi.org/10.1002/2015GL066996

Liu, Y., He, Q., Zhan, W., Guo, M., Zheng, Y., Shen, X., et al. (2025). Heterogeneity of phytoplankton response to submesoscale processes in the global ocean. Commun. Earth Environ., 6(1), 386. https://doi.org/10.1038/s43247-025-02365-3

Liu, Y., Zheng, Q., & Li, X. (2021). Characteristics of Global Ocean Abnormal Mesoscale Eddies Derived From the Fusion of Sea Surface Height and Temperature Data by Deep Learning. Geophys. Res. Lett., 48(17). https://doi.org/10.1029/2021gl094772

Luko, C. D., Lazaneo, C. Z., Silveira, I. C. A. d., Pereira, F., & Tandon, A. (2023). Topographically Generated Submesoscale Shear Instabilities Associated with Brazil Current Meanders. J. Phys. Oceanogr., 53(7), 1669-1689. https://doi.org/https://doi.org/10.1175/JPO-D-22-0122.1

Mahadevan, A. (2016). The Impact of Submesoscale Physics on Primary Productivity of Plankton. Annu. Rev. Mar. Science, 8(1), 161-184. https://doi.org/10.1146/annurev-marine-010814-015912

Mahadevan, A., Pascual, A., Rudnick, D. L., Ruiz, S., Tintoré, J., & D'Asaro, E. (2020). Coherent Pathways for Vertical Transport from the Surface Ocean to Interior. Bull. Am. Meteorol. Soc., 101(11), E1996-E2004. https://doi.org/https://doi.org/10.1175/BAMS-D-19-0305.1

Marshall, J., & Schott, F. (1999). Open-ocean convection: Observations, theory, and models. Rev. Geophys., 37(1), 1-64. https://doi.org/https://doi.org/10.1029/98RG02739

McWilliams, J. C. (2016). Submesoscale currents in the ocean. Proceedings of the Royal Society A: Mathematical, Physical and Engineering Sciences, 472(2189), 20160117. https://doi.org/10.1098/rspa.2016.0117

McWilliams, J. C. (2019). A survey of submesoscale currents. Geosci. Lett., 6(1), 3. https://doi.org/10.1186/s40562-019-0133-3

McWilliams, J. C. (2021). Oceanic Frontogenesis. Annu. Rev. Mar. Science, 13(Volume 13, 2021), 227-253. https://doi.org/https://doi.org/10.1146/annurev-marine-032320-120725

McWilliams, J. C., Gula, J., Molemaker, M. J., Renault, L., & Shchepetkin, A. F. (2015). Filament Frontogenesis by Boundary Layer Turbulence. J. Phys. Oceanogr., 45(8), 1988-2005. https://doi.org/https://doi.org/10.1175/JPO-D-14-0211.1

McWilliams, J. C., Molemaker, M. J., & Yavneh, I. (2004). Ageostrophic, anticyclonic instability of a geostrophic, barotropic boundary current. Physics of Fluids, 16(10), 3720-3725. https://doi.org/10.1063/1.1785132

Munk, W., Armi, L., Fischer, K., & Zachariasen, F. (2000). Spirals on the sea. Proceedings of the Royal Society of London. Series A: Mathematical, Physical and Engineering Sciences, 456(1997), 1217-1280. https://doi.org/10.1098/rspa.2000.0560

Napolitano, D. C., da Silveira, I. C. A., Tandon, A., & Calil, P. H. R. (2021). Submesoscale Phenomena Due to the Brazil Current Crossing of the Vitória-Trindade Ridge. J. Geophys. Res.: Oceans, 126(1), e2020JC016731. https://doi.org/https://doi.org/10.1029/2020JC016731

Ott, E. (2002). Chaos in Dynamical Systems (2 ed.). Cambridge University Press. https://doi.org/DOI: 10.1017/CBO9780511803260

Ottino, J. M. (1989). The kinematics of mixing: stretching, chaos, and transport (Vol. 3). Cambridge university press.

Peikert, R., Pobitzer, A., Sadlo, F., & Schindler, B. (2014). A Comparison of Finite-Time and Finite-Size Lyapunov Exponents. Topological Methods in Data Analysis and Visualization III, Cham.

Picard, T., Baker, C. A., Gula, J., Fablet, R., Mémery, L., & Lampitt, R. (2025). Estimating the variability of deep-ocean particle flux collected by sediment traps using satellite data and machine learning. Biogeosciences, 22(17), 4309-4331. https://doi.org/10.5194/bg-22-4309-2025

Poje, A. C., Özgökmen, T. M., Lipphardt, B. L., Haus, B. K., Ryan, E. H., Haza, A. C., et al. (2014). Submesoscale dispersion in the vicinity of the Deepwater Horizon spill. Proceedings of the National Academy of Sciences, 111(35), 12693-12698. https://doi.org/10.1073/pnas.1402452111

Prants, S. V., Budyansky, M. V., & Uleysky, M. Y. (2014). Identifying Lagrangian fronts with favourable fishery conditions. Deep Sea Res. Part I, 90, 27-35. https://doi.org/https://doi.org/10.1016/j.dsr.2014.04.012

Prend, C. J., Swart, S., Stewart, A. L., du Plessis, M. D., Manucharyan, G. E., & Thompson, A. F. (2025). Observed regimes of submesoscale dynamics in the Southern Ocean seasonal ice zone. Nat. Commun., 16(1), 8344. https://doi.org/10.1038/s41467-025-63775-7

Qu, L., Thomas, L., & Gula, J. (2021). Bottom Mixing Enhanced by Tropical Storm-Generated Near-Inertial Waves Entering Critical Layers in the Straits of Florida. Geophys. Res. Lett., 48(15), e2021GL093773. https://doi.org/https://doi.org/10.1029/2021GL093773

Rafiee, A. A., & Farhang, M. (2023). A deep convolutional neural network for salt-and-pepper noise removal using selective convolutional blocks. Appl. Soft Comput., 145, 110535. https://doi.org/https://doi.org/10.1016/j.asoc.2023.110535

Renault, L., Masson, S., Arsouze, T., Madec, G., & McWilliams, J. C. (2020). Recipes for How to Force Oceanic Model Dynamics. J. Adv. Model. Earth Syst., 12(2), e2019MS001715. https://doi.org/https://doi.org/10.1029/2019MS001715

Rocha, C. B., Gille, S. T., Chereskin, T. K., & Menemenlis, D. (2016). Seasonality of submesoscale dynamics in the Kuroshio Extension. Geophys. Res. Lett., 43(21), 11,304-311,311. https://doi.org/https://doi.org/10.1002/2016GL071349

Ruan, X., Wenegrat, J. O., & Gula, J. (2021). Slippery Bottom Boundary Layers: The Loss of Energy From the General Circulation by Bottom Drag. Geophys. Res. Lett., 48(19), e2021GL094434. https://doi.org/https://doi.org/10.1029/2021GL094434

Rudnick, D. L., & Ferrari, R. (1999). Compensation of horizontal temperature and salinity gradients in the ocean mixed layer. Science, 283(5401), 526-529. https://doi.org/10.1126/science.283.5401.526

Sasaki, H., Klein, P., Qiu, B., & Sasai, Y. (2014). Impact of oceanic-scale interactions on the seasonal modulation of ocean dynamics by the atmosphere. Nat. Commun., 5(1), 5636. https://doi.org/10.1038/ncomms6636

Schubert, R., Gula, J., Capó, E., Damien, P., Molemaker, M. J., Vic, C., et al. (2025). The ocean flows downhill near the seafloor and recirculates upward above. Nat. Commun., 16(1), 5873. https://doi.org/10.1038/s41467-025-61027-2

Schubert, R., Vergara, O., & Gula, J. (2023). The open ocean kinetic energy cascade is strongest in late winter and spring. Commun. Earth Environ., 4(1), 450. https://doi.org/10.1038/s43247-023-01111-x

Shchepetkin, A. F., & McWilliams, J. C. (2005). The regional oceanic modeling system (ROMS): a split-explicit, free-surface, topography-following-coordinate oceanic model. Ocean Modell., 9(4), 347-404. https://doi.org/https://doi.org/10.1016/j.ocemod.2004.08.002

Shcherbina, A. Y., D'Asaro, E. A., Lee, C. M., Klymak, J. M., Molemaker, M. J., & McWilliams, J. C. (2013). Statistics of vertical vorticity, divergence, and strain in a developed submesoscale turbulence field. Geophys. Res. Lett., 40(17), 4706-4711. https://doi.org/https://doi.org/10.1002/grl.50919

Siegelman, L., Klein, P., Rivière, P., Thompson, A. F., Torres, H. S., Flexas, M., et al. (2020). Enhanced upward heat transport at deep submesoscale ocean fronts. Nat. Geosci., 13(1), 50-55. https://doi.org/10.1038/s41561-019-0489-1

Spiro Jaeger, G., & Mahadevan, A. (2018). Submesoscale-selective compensation of fronts in a salinity-stratified ocean. Sci. Adv., 4(2), e1701504. https://doi.org/doi:10.1126/sciadv.1701504

Strobach, E., Klein, P., Molod, A., Fahad, A. A., Trayanov, A., Menemenlis, D., et al. (2022). Local Air-Sea Interactions at Ocean Mesoscale and Submesoscale in a Western Boundary Current. Geophys. Res. Lett., 49(7), e2021GL097003. https://doi.org/https://doi.org/10.1029/2021GL097003

Sullivan, P. P., & McWilliams, J. C. (2018). Frontogenesis and frontal arrest of a dense filament in the oceanic surface boundary layer. J. Fluid Mech., 837, 341-380. https://doi.org/10.1017/jfm.2017.833

Taylor, J. R., & Thompson, A. F. (2023). Submesoscale Dynamics in the Upper Ocean. Annu. Rev. Fluid Mech., 55(1), 103-127. https://doi.org/10.1146/annurev-fluid-031422-095147

Thomas, L. N., Tandon, A., & Mahadevan, A. (2008). Submesoscale Processes and Dynamics. In Ocean Modeling in an Eddying Regime (pp. 17-38). https://doi.org/https://doi.org/10.1029/177GM04

Thomas, L. N., & Taylor, J. R. (2010). Reduction of the usable wind-work on the general circulation by forced symmetric instability. Geophys. Res. Lett., 37(18). https://doi.org/https://doi.org/10.1029/2010GL044680

Thompson, A. F., Lazar, A., Buckingham, C., Naveira Garabato, A. C., Damerell, G. M., & Heywood, K. J. (2016). Open-Ocean Submesoscale Motions: A Full Seasonal Cycle of Mixed Layer Instabilities from Gliders. J. Phys. Oceanogr., 46(4), 1285-1307. https://doi.org/https://doi.org/10.1175/JPO-D-15-0170.1

Tozuka, T., & Cronin, M. F. (2014). Role of mixed layer depth in surface frontogenesis: The Agulhas Return Current front. Geophys. Res. Lett., 41(7), 2447-2453. https://doi.org/https://doi.org/10.1002/2014GL059624

Umlauf, L., & Burchard, H. (2003). A generic length-scale equation for geophysical turbulence models. J. Mar. Res., 61, 235-265.

Verma, V., Pham, H. T., & Sarkar, S. (2019). The submesoscale, the finescale and their interaction at a mixed layer front. Ocean Modell., 140, 101400. https://doi.org/https://doi.org/10.1016/j.ocemod.2019.05.004

Vic, C., Hascoët, S., Gula, J., Huck, T., & Maes, C. (2022). Oceanic Mesoscale Cyclones Cluster Surface Lagrangian Material. Geophys. Res. Lett., 49(4), e2021GL097488. https://doi.org/https://doi.org/10.1029/2021GL097488

Wang, Y., Curchitser, E., Legg, S., & Kang, D. (2025). Internal Tide Interactions with Submesoscale and Mesoscale Eddies in the Tropical Western Atlantic. J. Phys. Oceanogr. https://doi.org/https://doi.org/10.1175/JPO-D-24-0201.1

Whalen, C. B., & Drushka, K. (2025). Global distribution and governing dynamics of submesoscale density fronts. J. Phys. Oceanogr. https://doi.org/https://doi.org/10.1175/JPO-D-24-0119.1

Wilson, E. A., & Riser, S. C. (2016). An Assessment of the Seasonal Salinity Budget for the Upper Bay of Bengal. J. Phys. Oceanogr., 46(5), 1361-1376. https://doi.org/https://doi.org/10.1175/JPO-D-15-0147.1

Xing, Q., Yu, H., Wang, H., & Yu, H. (2023). A sliding-window-threshold algorithm for identifying global mesoscale ocean fronts from satellite observations. Prog. Oceanogr., 216, 103072. https://doi.org/https://doi.org/10.1016/j.pocean.2023.103072

Xing, Q., Yu, H., Yu, W., Chen, X., & Wang, H. (2025). A global daily mesoscale front dataset from satellite observations: in situ validation and cross-dataset comparison. Earth Syst. Sci. Data, 17(6), 2831-2848. https://doi.org/10.5194/essd-17-2831-2025

Yao, L., & Taylor, J. R. (2026). Global climatology of submesoscale restratification using machine learning. Sci. Rep. https://doi.org/10.1038/s41598-026-41929-x

Yao, L., Taylor, J. R., Jones, D. C., & Bachman, S. D. (2025). Identifying Ocean Submesoscale Activity From Vertical Density Profiles Using Machine Learning. Earth Space Sci., 12(1), e2022EA002618. https://doi.org/https://doi.org/10.1029/2022EA002618

Yoo, J. G., Kim, S. Y., & Kim, H. S. (2018). Spectral Descriptions of Submesoscale Surface Circulation in a Coastal Region. J. Geophys. Res.: Oceans, 123(6), 4224-4249. https://doi.org/https://doi.org/10.1029/2016JC012517

Yu, X., Barkan, R., & Naveira Garabato, A. C. (2024). Intensification of submesoscale frontogenesis and forward energy cascade driven by upper-ocean convergent flows. Nat. Commun., 15(1), 9214. https://doi.org/10.1038/s41467-024-53551-4

Zhang, Z., Liu, Y., Qiu, B., Luo, Y., Cai, W., Yuan, Q., et al. (2023). Submesoscale inverse energy cascade enhances Southern Ocean eddy heat transport. Nat. Commun., 14(1), 1335. https://doi.org/10.1038/s41467-023-36991-2

Zhang, Z., Qiu, B., Klein, P., & Travis, S. (2019). The influence of geostrophic strain on oceanic ageostrophic motion and surface chlorophyll. Nat. Commun., 10(1), 2838. https://doi.org/10.1038/s41467-019-10883-w